Cell Reports

Article

Multifold increase in spinal inhibitory cell types with emergence of limb movement

Graphical abstract

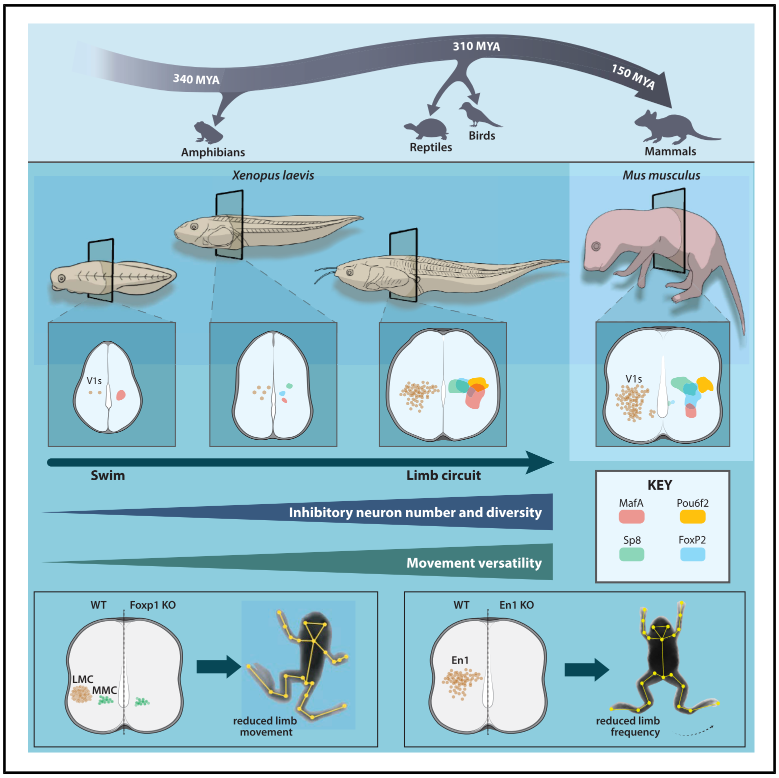

Highlights

- Kinematic and cellular basis of tadpole-to-frog motor circuit transformation
- V1 inhibitory neurons expand ~70-fold and diversify during tail-to-limb transition
- Motor and V1 inhibitory neuron subtypes conserved across vertebrates
- Engrailed-1 regulates V1 diversity and locomotor frequency across species and movement types

Authors

David Vijatovic, Florina Alexandra Toma,
Yuri Ignatyev, ..., Jeremy S. Dasen,
Jay B. Bikoff, Lora B. Sweeney

Correspondence

lora.sweeney@ist.ac.at

In brief

Frog metamorphosis reveals how spinal circuits adapt to new motor demands. Vijatovic et al. demonstrate that the shift from tail- to limb-based locomotion coincides with expansion and diversification of V1 inhibitory neurons. Cross-species comparisons identify a conserved blueprint of tail and limb locomotion, with Engrailed-1 a global regulator of movement frequency.

Vijatovic et al., 2026, Cell Reports *45*, 117227
April 28, 2026
https://doi.org/10.1016/j.celrep.2026.117227

CellPress

Cell Reports

CellPress
OPEN ACCESS

Article

Multifold increase in spinal inhibitory cell types with emergence of limb movement

David Vijatovic,[1] Florina Alexandra Toma,[1] Yuri Ignatyev,[1] Zoe P.M. Harrington,[1] Christoph Sommer,[1] Robert Hauschild,[1] Matthjis Smits,[1] Marco Dalla Vecchia,[1] Alexandra J. Trevisan,[2] Phillip Chapman,[2] Mara J. Julseth,[1] Susan Brenner-Morton,[3] Mariano I. Gabitto,[4,5] Jeremy S. Dasen,[6] Jay B. Bikoff,[2] and Lora B. Sweeney[1,7,8,*]

[1]Institute of Science and Technology Austria, Klosterneuburg, Austria
[2]Department of Developmental Neurobiology, St. Jude Children's Research Hospital, Memphis, TN, USA
[3]Zuckerman Institute, Columbia University, New York, NY, USA
[4]Allen Institute for Brain Science, Seattle, WA, USA
[5]Department of Statistics, University of Washington, Seattle, WA, USA
[6]NYU Neuroscience Institute, Department of Neuroscience and Physiology, NYU School of Medicine, New York, NY, USA
[7]Senior author
[8]Lead contact
*Correspondence: lora.sweeney@ist.ac.at

https://doi.org/10.1016/j.celrep.2026.117227

SUMMARY

As vertebrates transitioned from water to land, locomotion shifted from undulatory swimming to limb-based movement. How spinal circuits and their cell types evolved to support this transition remains unclear. We leverage frog metamorphosis, which recapitulates this transition within a single organism, to define how spinal circuits generate aquatic versus terrestrial motor patterns. At swim stages, spinal architecture is uniform, with a transcriptionally and anatomically homogeneous motor and interneurons. As limbs develop and their movement complexifies, spinal circuits expand in neuron number and subtype diversity. This expansion is most pronounced for V1 inhibitory neurons, which increase ∼70-fold and diversify into transcriptionally distinct subtypes. Disrupting transcription factors defining emerging motor and V1 populations reveals molecular segregation between swim and limb circuits, highlighting the role of subtype diversity in motor coordination. A multifold increase in inhibitory neuron diversity thus underlies the tail-to-limb locomotor transition, providing a framework for spinal circuit adaptation during vertebrate evolution.

INTRODUCTION

In vertebrates, spinal neurons serve as the final relay driving the dynamic patterns of muscle contraction that underlie diverse motor behavior. Jawless fish, most bony fish, and larval amphibians move via alternating contraction of left-right axial musculature, producing undulatory swimming.[1] Limbed vertebrates, in contrast, rely on coordination of flexor-extensor muscles within and across limbs to generate a wide range of movements, including walking, running, trotting, and hopping.[2,3] Both swim and limb motor patterns are governed by complex networks of interneurons in the ventral spinal cord that regulate motor neuron (MN) activity.[4,5] While select aspects of spinal circuit architecture are conserved across vertebrates, it is still unclear how these networks adapt to differentiate aquatic versus terrestrial motor programs.

Comparative analysis of vertebrate spinal circuits has raised the hypothesis that increased cell type heterogeneity is essential for refining and diversifying motor outputs across species,[6] a hypothesis that is as of yet largely untested. In zebrafish, swimming is controlled by a relatively simple spinal network of MNs and interneurons, subdivided into slow, intermediate, and fast types, to regulate locomotor speed.[7,8] In mammals, by contrast, motor behavior is more complex, and spinal neuron diversity appears to reach its apogee, with six cardinal neuron classes in the ventral spinal cord. Each class is defined by a unique transcriptional program and, as exemplified by ventral V1,[9–12] V2a,[13,14] and V3[15,16] interneurons, further subdivided into dozens of subtypes according to their physiology, connectivity, and neurotransmitter expression.[4,17,18]

Among ventral classes, V1 inhibitory interneurons, which provide over 50% of inhibitory inputs onto MNs,[19] stand out for their exceptionally high diversity, comprising at least four clades and over 50 predicted cell types based on the combinatorial expression of 19 transcription factors (TFs).[9,10,20] V1 subtypes are further specialized along the length of the spinal cord, with distinct transcriptional profiles at limb versus non-limb segments.[11] How this extensive cell type heterogeneity maps onto motor function remains unclear. Which aspects of spinal cell type diversity are fundamental for all vertebrate movement, and which are specific for limb control?

The African clawed frog, *Xenopus laevis*, which transitions from swim- to limb-based locomotion during metamorphosis, provides a unique opportunity to address these questions

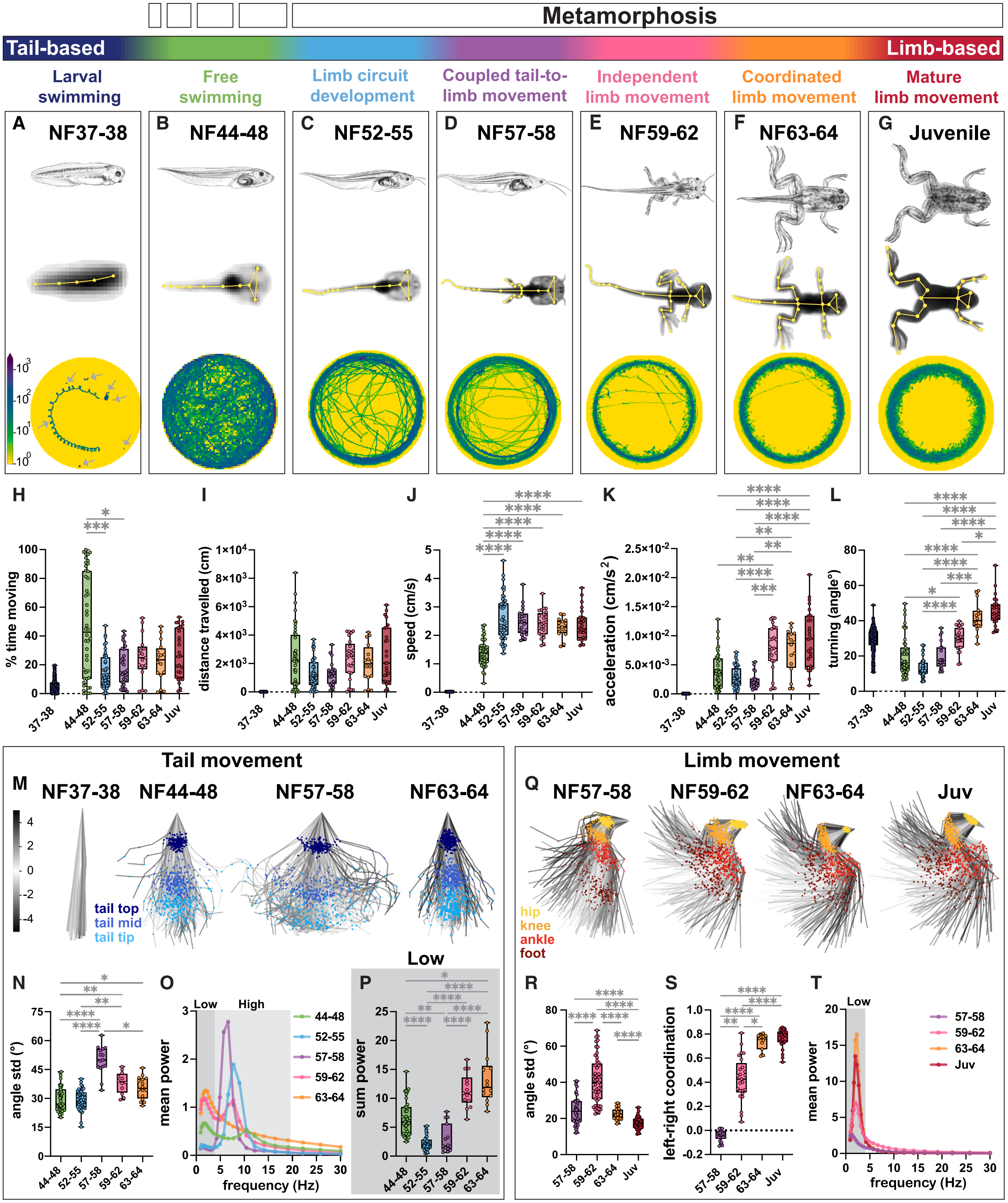

Figure 1. Loss of tail and emergence of limb movement during frog metamorphosis

(A–G) Stages of frog metamorphosis, spanning the transition from tail- to limb-based movement, are divided into seven bins according to their anatomical features, motor function, and underlying circuitry (Nieuwkopp and Faber [NF][26]): larval swimming (A, NF37–38, dark blue), free swimming (B, NF44–48, green), limb circuit development (C, NF52–55, blue), and coupled tail-to-limb (D, NF57–58, purple), independent (E, NF59–62, pink), coordinated (F, NF63–64, orange),

(legend continued on next page)

within a single organism. During a 2-month period, motor behavior rapidly transforms from undulatory escape to free swimming and finally to coordinated limb movements such as walking, hopping, and scooping.[21–23] How this metamorphic transformation unfolds, to what extent spinal neuron identities change, and how these changes shape distinct locomotor patterns remain largely unknown. Uncovering these principles in the frog will yield generalizable insight into how cell type diversification supports the sophistication of motor behaviors.

Here, we perform a longitudinal analysis of locomotor behavior and spinal cord cell types across frog metamorphosis to define the neural architecture underlying swimming versus limb motor control. We generate a high-resolution behavioral atlas of the swim-to-limb transition that reveals a progressive increase in the complexity of motor patterns. In parallel, we use single-cell sequencing to profile spinal cord cell types and track their heterogeneity during metamorphosis. Across both swim and limb stages, the core organization of spinal circuits comprises all cardinal ventral neuron classes. Among these, V1 inhibitory interneurons exhibit the most dramatic expansion at limb stages. Their number and molecular diversity scale up with increasing motor complexity, culminating in dozens of molecularly and positionally distinct subtypes defined by TF expression. CRISPR-Cas9-based loss of function of the hallmark TFs FoxP1 and Engrailed-1 (En1), expressed by MNs and V1s, respectively, disrupts both cell identity and locomotor output, differentiating patterns of swim and limb movement. Our findings thus demonstrate that increased inhibitory neuron heterogeneity is a determinant feature of spinal circuits for limb-based locomotion.

RESULTS

Frog metamorphosis captures complexification and remodeling of motor behavior in one species

Frog metamorphosis provides a unique opportunity to isolate the behavioral and cellular units of swimming versus limb movement in a single organism and to evaluate how one locomotor mode transforms into another. We thus devised an assay to quantify locomotion in freely moving *X. laevis* tadpoles and frogs using SLEAP deep-learning pose estimation (STAR Methods; Figures 1A–1G and S1A–S1D).[24,25] The tadpole-to-frog transition was divided into seven developmental bins spanning the shift from tail- to limb-based locomotion: larval-swimming (Nieuwkopp and Faber [NF] 37–38), free-swimming (NF44–48), and five metamorphic stages, further subdivided according to limb anatomy, function, and emergent changes in spinal circuits (NF52-juvenile; Figures 1A–1G).[26–28] Two high-precision SLEAP models were generated per bin to track the animal's center point, tail, and limb positions (STAR Methods; Figures S1C and S1D).

As tadpoles transitioned to frogs, they acquired varied movement patterns (Figures 1A–1L and S1E). Larval-swimming tadpoles first scarcely moved, covering only short distances at low speed and acceleration (Figures 1A, 1H–1K, and S1E; Video S1), consistent with a previous report.[30] As tadpoles transitioned to free swimming, their time spent moving, distance, speed, and acceleration increased (Figures 1B, 1H–1K, and S1E; Video S2). This highly active movement persisted throughout metamorphosis, with animal displacement constant, high-speed movement maintained and acceleration further increasing with emergence of limb movement (Figures 1C–1G and 1H–1K). In addition, metamorphosis was also accompanied

and mature (G, juvenile, red) limb movement. Metamorphic stages and the switch from tail-based to limb-based locomotion are also indicated. For each stage: schematic of tadpole anatomy (top row, adapted from *Xenopus* illustrations, © Natalya Zahn, 2022[29]); SLEAP skeleton (yellow) superimposed onto an image of a recorded animal (A–G, middle row), and example of the distance traveled by seven (A, bottom row, arrows individual animals) or individual animal (B–G, bottom row). Tadpoles are mostly stationary at larval swim stages (A), explore the whole dish from free-swimming stages (B), and then transition to edge tracking with the emergence of limbs (B–G).

(H–L) Quantification of tadpole and frog movement. The percentage of time spent moving shows that NF52–58 animals move less than at the free-swimming stage; movement is then constant across later stages (H). Distance traveled is constant across all stages of metamorphosis (I). Mean speed is the lowest at NF44–48, increases by NF52–55, and then remains constant (J). Acceleration subdivides into two modes: low from tail-based NF44 to NF58 and high from limb-based NF59 to juvenile stages (K). Turning, calculated as the mean directional change of the animal's trajectory, increases stepwise with limb movement across metamorphosis, peaking at juvenile stage (L, 0° angle is parallel indicating no turning). Kruskal-Wallis test was used for (H)–(L); *$p < 0.05$, **$p < 0.01$, ***$p < 0.001$, ****$p < 0.0001$.

(M–P) Range and frequency of tail movement across tadpole metamorphosis. Principal-component analysis (PCA) plots of tail position across 256 random frames represent its range of movement (M; tail top, dark blue; tail mid, blue; tail tip, light blue). Tail movement first increases and then decreases during the transition from tail- to limb-based stages (M). Quantification of the range of movement of the tail tip shows a peak at NF57–58 and a decrease from NF59–64 as the tail recedes (N). Mean power spectrum of frequency of tail tip oscillations for each stage of metamorphosis, with low (0.9–4.5 Hz, dark gray) and high (4.5–20 Hz, light gray) frequency bins highlighted (O). From NF44–48 to NF59–62, the frequency spectrum is bimodal with a peak in the low and high frequency bins; at NF63–64, it is unimodal with only one low frequency peak (O). The amount of tail tip movement in the low-frequency bin, represented by the sum power, decreases from NF44–48 to NF52–55 and then increases until NF63–64 (P). Kruskal-Wallis test was used for (N) and (P). *$p < 0.05$, **$p < 0.01$, ****$p < 0.0001$.

(Q–T) Gain of hindlimb movement during frog metamorphosis. PCA plots represent the position of the hindlimb and its range of movement during 256 random frames, showing an increase in range from NF57–58 to NF59–62 (Q; hip, yellow; knee, orange; ankle, red; foot, brown). Quantification of the range of knee movement shows an initial increase from NF57–58 to NF59–62 and then a decrease until juvenile stage (R). Coordination of the left and right knees changes from random at NF57–58 to bilaterally synchronous at NF63–64 (S; +1 = synchronous, 0 = random, −1 = alternating). The mean power spectrum of the knee oscillations for each stage of metamorphosis shows a single peak in the low-frequency range (T; 0.9–4.5 Hz, dark gray). Brown-Forsythe and Welch ANOVA tests were used for (R); Kruskal-Wallis test was used for (S). *$p < 0.05$, **$p < 0.01$, ****$p < 0.0001$.

$n = 172$ animals for NF37–38, $n = 47$ animals for NF44–48, $n = 24$ animals for NF52–55, $n = 11$ animals for NF57–58, $n = 13$ animals for NF59–62, $n = 8$ animals for NF63–64, $n = 13$ animals for juvenile stage. The scale bar in (A) indicates the number of times the animal was present in a specific area of the dish (10° frames, yellow to 10^3 frames, blue). Statistics in (H)–(L) were applied to all stages excluding NF37–38, as indicated by the broken axis. The scale bar in (M) indicates the color code of the first principal component of variation of the aligned tail and limb positions in (M) and (Q).

by a stepwise increase in the amount of turning, as tadpoles switched from exploring the whole dish to preferentially tracking its edge (Figures 1C–1G, 1L, and S1E; Video S3–S7).[31] Our analysis thus defines phases of tail- to limb-based locomotion, characterized by variant propulsion and directionality of movement.

To determine the kinematic changes that underlie these metamorphic phases of locomotor behavior, we analyzed the movement of the tail, hindlimbs, and forelimbs. The range of tail movement, initially restricted in larval swimming, peaked at initial stages of metamorphosis and then decreased as limb coordination emerged (Figures 1M, 1N, S2A, and S2B). The frequency of tail oscillation also shifted from proportional low- and high-frequency at free swimming to majority high frequency at early metamorphic stages and then to only low-frequency oscillations at the final stages of metamorphosis (low frequency: 0.9–4.5 Hz; high frequency: 4.5–20 Hz; Figures 1O, 1P, S1F–S1H, and S2E–S2I). Thus, as the tail receded and limb coordination emerged, the tail frequency matched the frequency of the hindlimbs (~2.2 Hz; Figures S2D and S2I versus S2O).

During metamorphosis, complex limb movement emerged, as revealed by three main kinematic features. First, with the transition to independent limb movement,[27] the angle and range of both the hind- and forelimbs increased; then, as limbs further developed and motor control increased at late metamorphic stages,[26,27] their range decreased in magnitude (Figures 1Q, 1R, S1I, S1L–S1N, S2J, and S2K). Second, left-right hindlimb synchrony, which was absent at the coupled tail-to-limb movement stages, increased in a stepwise manner across metamorphosis (Figures 1S and S2L), consistent with the emergence of bilateral kicking, the dominant form of movement of mature *Xenopus*[23] and many other frogs.[32] Third, the frequency of hind- and forelimb oscillations gradually increased in magnitude and power (Figures 1T, S1J, S1K, S1O–S1Q, and S2M–S2Q), initially matching the tail at ~1.5 Hz (Figures S2C and S2G versus S2M) and later shifting to ~2.2 Hz (Figure S1K, S1Q, and S2N–S2P), the approximate step frequency of mouse limbs.[33] Limbs are thus initially coupled to the tail rhythm, consistent with previous electrophysiological observations,[34] and, as the tail recedes, gain the ability to drive independent, synchronous, and fine-scale movement.

This increased complexity of limb movement across metamorphosis coincided with an increase in turning behavior (Figure 1L), raising the question of how changes in motor pattern affect limb kinematics. To address this, we subsampled our videos to isolate straight-line forward movement episodes (Figures S3A–S3C; STAR Methods). Across all joints, the mean angle of the limb as well as the range and frequency of limb movement demonstrated similar metamorphic transformation between straight-line and total moving episodes (Figures S3D, S3E, and S3G–S3L). In addition, during straight-line episodes, near-perfect left-right synchronous kicking was reached across all hindlimb joints (Figures S3F versus 1S and S2L), consistent with increased synchrony generating straight line movement. This supports the generalizability of observed limb kinematics across movement types.

Our kinematic analysis thus defines tail- and limb-based locomotor phases of frog metamorphosis with features, rhythms, and coordination patterns of increasing complexity. Across this transformation, we not only characterize loss-of-tail and gain-of-limb coordination but also show initial limb-to-tail and later tail-to-limb rhythmic coupling at intermediate stages. These behavioral insights yield an entry point to determine the spinal circuits and cell types that drive and modulate each locomotor program.

Spinal cell type profiling identifies inhibitory interneuron enrichment in limb circuits

Multiple cellular mechanisms could underlie this swim-to-limb transformation and drive the corresponding increase in movement complexity. To orchestrate emergent limb movement patterns, existing cell types in the spinal cord could be repurposed, or additional neurons could be added of the same or different cell types. Distinguishing between these mechanisms using frog metamorphosis will offer fundamental insight into the cellular underpinnings of aquatic versus terrestrial locomotion.

To evaluate how spinal cord cellular composition varies across locomotor phases of metamorphosis, we generated a developmental time course of cell type emergence, focusing on MNs (Figure S4A, S4B, S4E, S4F, and S4I–S4K) and one representative population of motor-related interneurons (Figure S4C, S4D, S4G, S4H, and S4L–S4O). Peak MN cell numbers and subtype diversity were observed between NF54 and NF56, metamorphic stages with prominent limbs but no limb-based locomotion,[26] whereas peak interneuron numbers extended from NF54 to NF64, spanning the period of limb movement refinement. To parse the relationship between these emerging cell types and motor behavior, we performed single-cell RNA sequencing at four landmark stages of tadpole-to-frog development: larval swim stages (NF37–38), free-swimming stages (NF44–47), and two peak stages of limb circuit development: NF54–55, a representative time point of maximal spinal neuron number, and NF57–58, the time point of initial limb movement (Figures 2A–2D).[28,35–39] Spinal cord cells were isolated from *tubb2b:GFP* transgenic tadpoles, in which GFP was selectively expressed in all postmitotic neurons.[40–42] At each stage, we obtained at least 20,000 cells with an average of ~3,200 genes per cell after quality control filtering (STAR Methods). Neurons, enriched by fluorescence-activated cell sorting, were further identified by post hoc analysis of neural gene expression patterns (STAR Methods). Expression of pan-neuronal (*tubb2b*, *elavl3/4*, and *snap25*), excitatory (*slc17a7*), inhibitory (*gad2*), and cholinergic (*slc18a3*) marker genes confirmed robust isolation of neurons at each stage (Figures S5A–S5D).

In-depth analysis of neural cell type diversity revealed that all 12 cardinal classes (MNs, V0–V3, and dI1–dI6) were present across developmental stages, spanning the full transition from tail- to limb-based locomotion (Figures 2A–2D and S5E–S5H). This high conservation demonstrated that basic cardinal subdivisions are a shared foundation for both swim and limb locomotor programs. However, with the acquisition of limbs, the ratio of interneurons to MNs increased nearly 15-fold, from ~5:1 to ~70:1 (Figures 2E and S5I). This shift indicates that limb motor control requires amplified circuit regulation by interneurons added to a shared core architecture.

Given the differences in rhythm and coordination of the tail versus limb between tadpoles and frogs, we hypothesized that ventral interneurons, key drivers of locomotor pattern in mammals,[43] may increase in proportion during the swim-to-limb transition. We thus focused our analysis on the six ventral cardinal

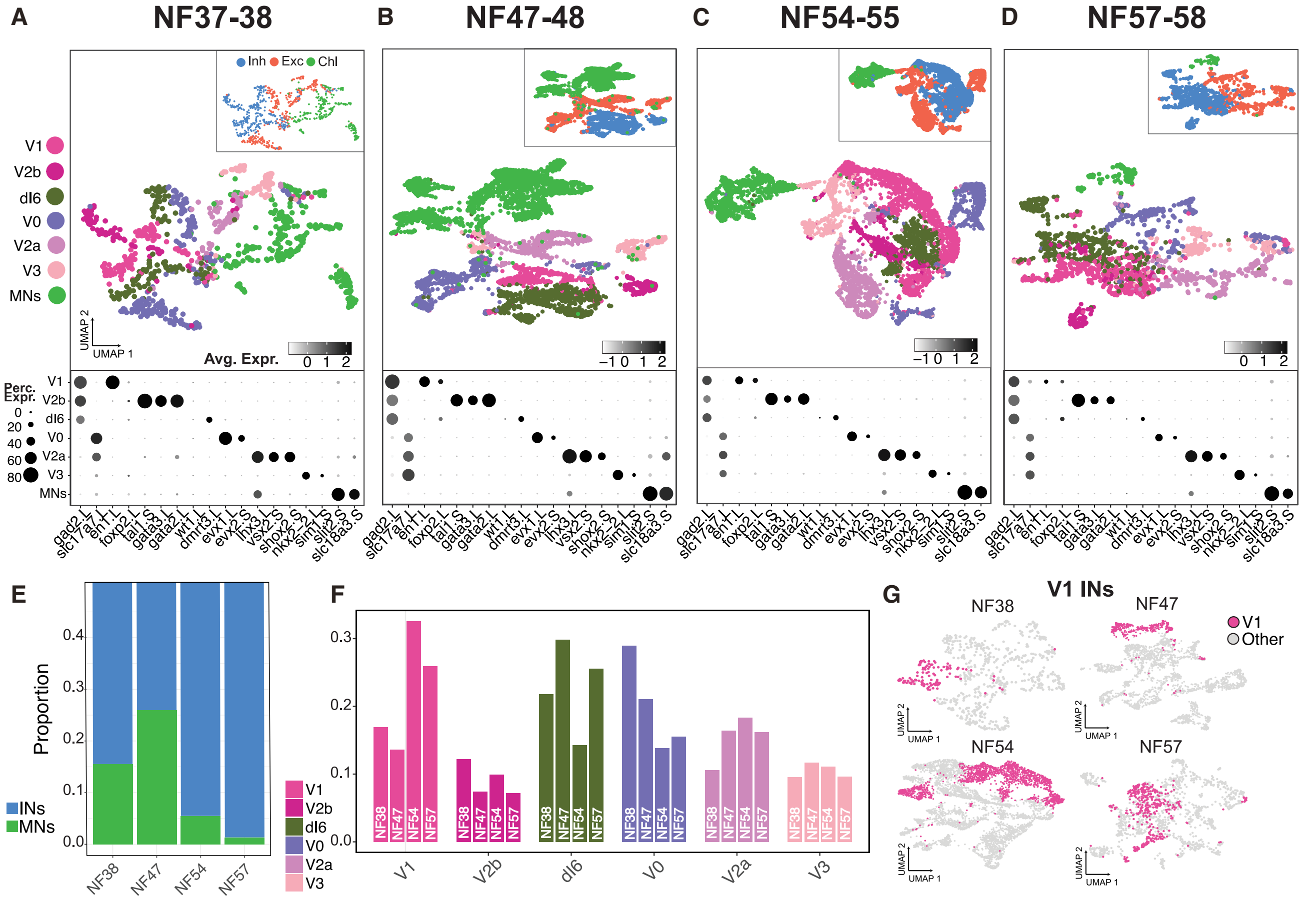

Figure 2. Selective enrichment of V1 inhibitory neurons during frog metamorphosis

(A–D) UMAP representation (top) and gene expression dot plots (bottom) of rhythm-generating cardinal classes of interneurons (V1, V2b, dI6, V0, V2a, and V3) and motor neurons (MNs) across four stages of tadpole-to-frog metamorphosis: swim stages NF37–38 (A) and NF47–48 (B) and limb stages NF54–55 (C) and NF57–58 (D).

(E) Proportion of MNs (blue) versus spinal interneurons (INs; green) from NF38 to NF57.

(F) Proportion of each cardinal class involved in rhythm generation relative to total ventral INs (V1, V2b, dI6, V0, V2a, and V3) by metamorphic stage.

(G) UMAP representation of ventral INs from (A)–(D), highlighting the V1 inhibitory cardinal class population (magenta), as identified by the expression of *en1* and *foxd3* (Figure S5).

classes (excitatory V0v, V2a, and V3 and inhibitory V1, V2b, and dI6 neurons; Figures 2F and S5J), tracking how they changed based on their unique transcriptional signatures. Analysis of the population proportion by stage surprisingly revealed a selective enrichment at limb stages of V1 inhibitory neurons (Figures 2F, 2G, S5J, and S5K), marked by the expression of *en1*.[44,45]

A conserved neuronal organization of the ventral horn, consisting of MNs and six interneuron classes, thus emerged from our transcriptomic analysis as a shared foundation for both swim and limb locomotor programs. However, whether the increasing complexity of limb-based movement required additional subtype specialization within these broad classes remained unclear.

Diversification of MN cell types underlies metamorphic behavioral switch

To begin to address this question, we first focused on MNs, as they were present across all developmental stages (Figures 2A–2D and S4), have well-characterized molecular and functional organization, and serve as the final neural relay between the spinal cord and muscles.[5] These features made MNs an ideal starting point to evaluate how spinal circuits adapt to generate increasingly complex movements during metamorphosis.

To investigate how MN identity changes during the swim-to-limb transition, we performed immunohistochemical analysis of MNs at the same three landmark periods of tadpole development. At all stages, we identified a ventral population of spinal neurons co-expressing the MN determinants Isl1 and Mnx1/Hb9 (Figures 3A–3D, S6A, and S6B).[46–49] Larval swim circuits were small and simple, with ~5 MNs per 15 μm spinal cord section (Figures 3A and 3D), as previously observed with dye fills.[50] MN number then doubled with the transition to free swimming (Figures 3B, 3D, S6A, and S6B). Metamorphosis further resulted in a dramatic expansion of the MN population, with an additional 10-fold increase in number at limb and 5-fold increase at thoracic levels (Figures 3C and 3D), marking the

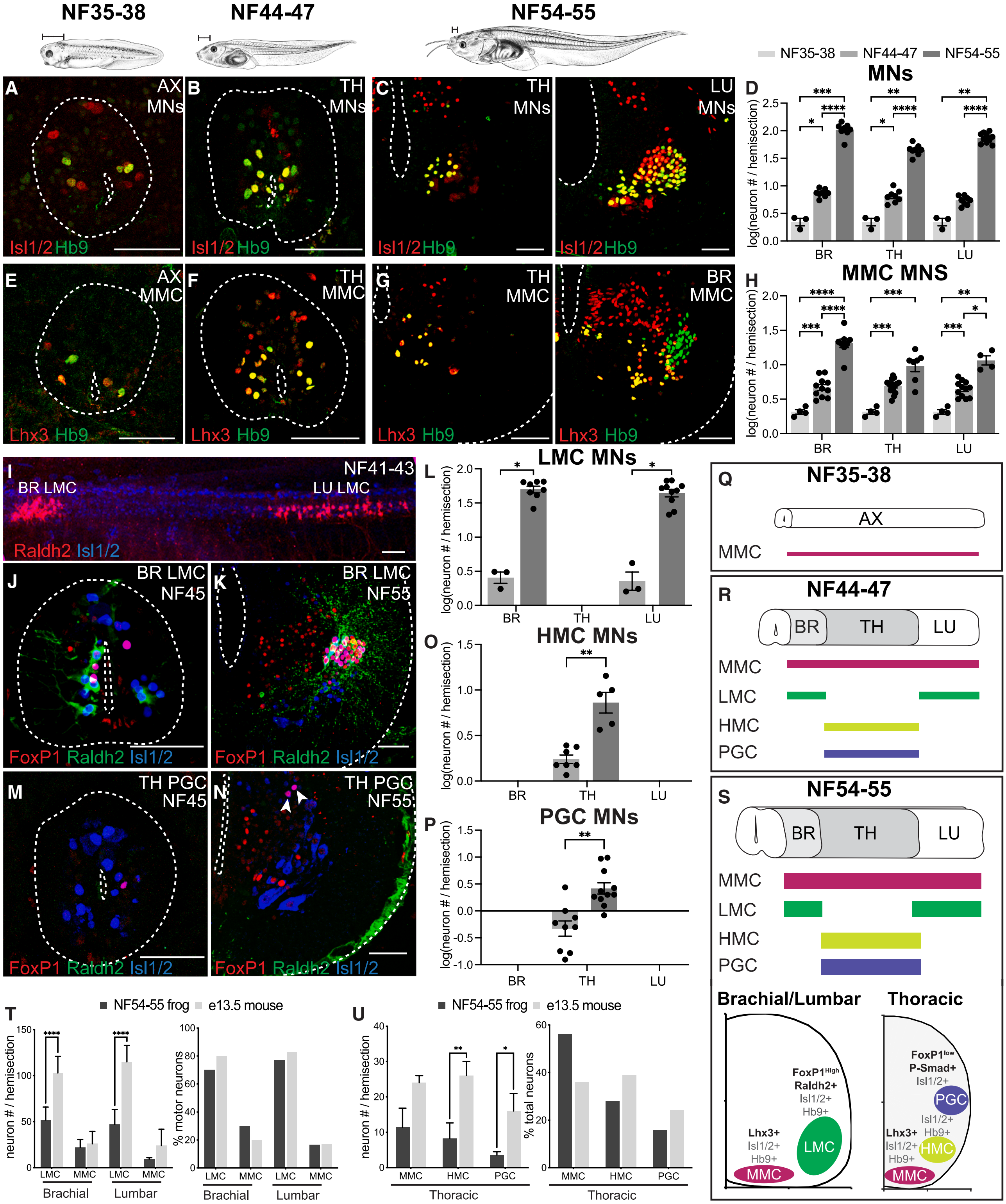

Figure 3. Spinal MNs expand and diversify during *Xenopus* frog metamorphosis

(A–D) MN number increases during metamorphosis. MNs in the axial (AX), thoracic (TH), and lumbar (LU) spinal cord express the pan-MN markers Hb9 (green) and Isl1/2 (red) and increase in number between NF35–38 (A), NF44–47 (B), and NF54–55 (C). The bar graph (D) shows the total number of $Hb9^+$ $Isl1/2^+$ (NF37–38 and NF44–47) or ventral $Isl1/2^+$ (NF54–55) MNs per 15 μm ventral horn (mean ± SEM for 3–10 animals) of the brachial (BR), TH, and LU spinal cord. Brown-Forsythe and Welch ANOVA tests were used for (D). $*p < 0.05$, $**p < 0.01$, $***p < 0.001$, $****p < 0.0001$.

(legend continued on next page)

peak of MN and limb motor circuit development (Figure S4A, S4B, and S4E–S4G).[26]

In mammals, MNs are organized into four columnar classes and further subdivided along the rostrocaudal, dorsoventral, and mediolateral axes into flexor-extensor divisions and ∼50 motor pools.[5] We thus evaluated whether this well-defined MN architecture was conserved in frogs and when it emerges during metamorphosis. We found that MN columns, divisions, and pools, distinguished by TF expression, are added sequentially during metamorphosis. MNs in early larval tadpoles uniformly co-expressed Hb9 and Lhx3 (Figures 3E and 3H),[52] establishing their medial motor column (MMC) identity.[53,54] These MMC neurons doubled in number by free-swimming stages (Figures 3F and 3H), coinciding with increased swimming (Figure 1), and later peaked during metamorphosis (Figures 3G and 3H), paralleling the growth and patterning of axial musculature.[55]

Thoracic spinal circuits also transformed during the swim-to-limb transition. Preganglionic column (PGC)-like MNs, known to innervate the sympathetic chain ganglia and regulate visceral organs, are identified by expression of FoxP1, pSmad, and Isl1.[56] PGC neurons first emerged at free-swimming stages and then expanded during metamorphosis (Figures 3M, 3N, 3P, S6B, and S6F), coinciding with the development of internal organs in tadpoles.[57] Similarly, the hypaxial motor column (HMC), defined by co-expression of Isl1 and Hb9 and the absence of other columnar identifiers,[56] was restricted to thoracic levels and doubled in number at metamorphosis (Figure 3O). In mice, HMC neurons innervate hypaxial trunk muscles involved in respiration and postural control during locomotion.[58]

The most prominent change to MNs was identified at limb levels during metamorphosis. As limbs developed, a large population of lateral motor column (LMC) neurons emerged: bearing striking molecular similarity to those in amniotes,[52,56,59] positioned in the ventrolateral brachial and lumbar spinal cord, and expressing the canonical LMC markers, FoxP1 and Raldh2/Aldh1a2[60] (Figures 3K and 3L). This LMC population was subdivided into medial and lateral divisions (Figures S6C and S6D), a FoxP1$^+$Raldh2$^-$ subset resembling digit-innervating MNs,[61] and a rostrocaudally restricted cScip/Pou3f1$^+$ group akin to the flexor carpi ulnaris motor pool (Figure S6E).[62] Surprisingly, at free-swimming stages, prior to visible limb formation, we identified two LMC-like populations that we termed pioneering LMC. These neurons expressed FoxP1 and Raldh2 (Figures 3I, 3J, and 3L) and projected toward the site of future limb bud (Figure 4J). These pioneering neurons were absent from larval swim circuits (Figures S6G and S6H) and may constitute a proto-circuit that facilitates the later development and integration of limb-innervating MNs during metamorphosis.

We thus demonstrate that the addition of MN columns, divisions, and subtypes is a hallmark feature of spinal circuit transformation during metamorphosis. This raises the question of how these subtypes relate to the generation of four-limb movement across species. To address this question, we compared MN composition in frogs and mice at analogous stages of limb circuit development: NF54–55 tadpoles (Figures S4A–S4K) and embryonic day 13.5 (E13.5) mice.[51] Tadpoles had approximately half as many MNs per column as mice, but the relative proportions of each subtype were highly conserved (Figures 3T and 3U). At limb levels, MNs were ∼80% LMC and ∼20% MMC in both species, while thoracic MNs were composed of ∼45% MMC, ∼35% HMC, and ∼20% PGC. This contrasted with earlier tadpole stages. At larval swim stages, 100% of MNs were of the MMC type (Figure S6H), and at free-swimming stages, ∼60% were MMC and ∼40% were either LMC or HMC/PGC (Figures S6I and S6J). These data demonstrate a progressive expansion and specialization of MNs from a simple swim-specific to a conserved, mouse-like limb circuit architecture in frogs (Figures 3Q–3S). We thus show high conservation of MN transcriptional identity and the gradual emergence of limb-associated MN subtypes during metamorphosis.

(E–H) The medial motor column (MMC) emerges in larval *Xenopus* and expands during metamorphosis. The antibody against the Lhx3 transcriptional determinant of MMC identity (red) labels a subset of Hb9$^+$ MNs (green) in the spinal cord of NF35–38 (E), NF44–47 (F), and NF54–55 (G) tadpoles. Shown are AX (NF35–38), TH (NF44–47 and NF54–55) and brachial (NF54–55) sections (see Figure S6 for the images of additional immunolabeled TH, BR, and LU sections). The graph (H) shows the number of Lhx3$^+$ Hb9$^+$ MMC MNs per 15 μm ventral horn (mean ± SEM for 4–14 animals) at BR, TH, and LU levels at NF35–38, NF44–47, and NF54–55. Brown-Forsythe and Welch ANOVA tests were used for (H). *$p < 0.05$, **$p < 0.01$, ***$p < 0.001$, ****$p < 0.0001$.

(I–P) The lateral motor column (LMC), preganglionic motor column (PGC), and hypaxial motor column (HMC) emerge in free-swimming tadpoles and expand during metamorphosis. A side view of an NF41–43 spinal cord (I) stained for the LMC determinant Raldh2 (red) and Isl1/2 (blue) reveals the nascent BR and LU populations of limb-innervating MNs. The LMC determinants FoxP1 (red) and Raldh2 (green) jointly label an MN subset (Isl1/2, blue) at BR and LU levels at NF44–47 (J) and NF54–55 (K). The number of LMC MNs (L) per 15 μm ventral horn (mean ± SEM for 3–10 animals) of BR, TH, and LU segments at NF44–47 and NF54–55. Frog PGC MNs are labeled by the PGC transcriptional determinants FoxP1 (red) and Isl1/2 (blue) at TH levels at NF44–47 (M) and NF54–55 (N). Neither the LMC nor PGC is present at NF35–38 (Figures S6G–S6J). The number of HMC (O) and PGC (P) MNs per 15 μm ventral horn (mean ± SEM for 5–11 animals) of BR, TH, and LU levels at NF44–47 and NF54–55. HMC MN number at the TH level was calculated by subtracting the number of MMC and PGC MNs from the total number of MNs. Kruskal-Wallis test was used for (L); Welch's *t* test was used for (O); and Mann-Whitney test was used for (P). *$p < 0.05$, **$p < 0.01$.

(T and U) Conservation of MN proportions in developing limb circuits of frogs and mice. Number of LMC and MMC MNs (left) and their percentage (right) in the total MN population at BR and LU levels (T) at frog NF54–55 and mouse E13.5. Number of HMC, PGC, and MMC MNs (left) and their percentage (right) in the total MN population at the TH level (U) at frog NF54–55 and mouse E13.5 stages. Shown is the mean ± SEM for 5–11 animals. The embryonic mouse counts were extracted from Agalliu et al.,[51] with the SEM estimated from the provided plots. Two-way ANOVA with Šídák multiple comparisons test was used for (T) and (U). *$p < 0.05$, **$p < 0.01$, ****$p < 0.0001$.

(Q–S) Summary of MN development in tadpoles. Schematics show the rostrocaudal distribution of MMC (Lhx3$^+$, Isl1/2$^+$, and Hb9$^+$), HMC (Isl1/2$^+$ and Hb9$^+$), and PGC (FoxP1^{low}, Raldh2$^+$, Lhx3$^+$, Isl1/2$^+$, and Hb9$^+$) subsets in NF35–38 (Q), NF44–47 (R), and NF54–55 (S, top) spinal cords. Schematized spinal cord hemi-section of a limb and TH segment depicts the relative position and molecular markers of each motor column along the dorsoventral, mediolateral axis (S, bottom).

Shown is either a spinal cord cross-section (NF35–38/44–47) or a ventral hemi-section (NF54–55) with the central canal and outer edge indicated (dotted line). Scale bar in micrographs, 50 μm (except in I, 100 μm) and in drawings, 1 mm. Tadpole drawings adapted from *Xenopus* illustrations © Natalya Zahn (2022).[29]

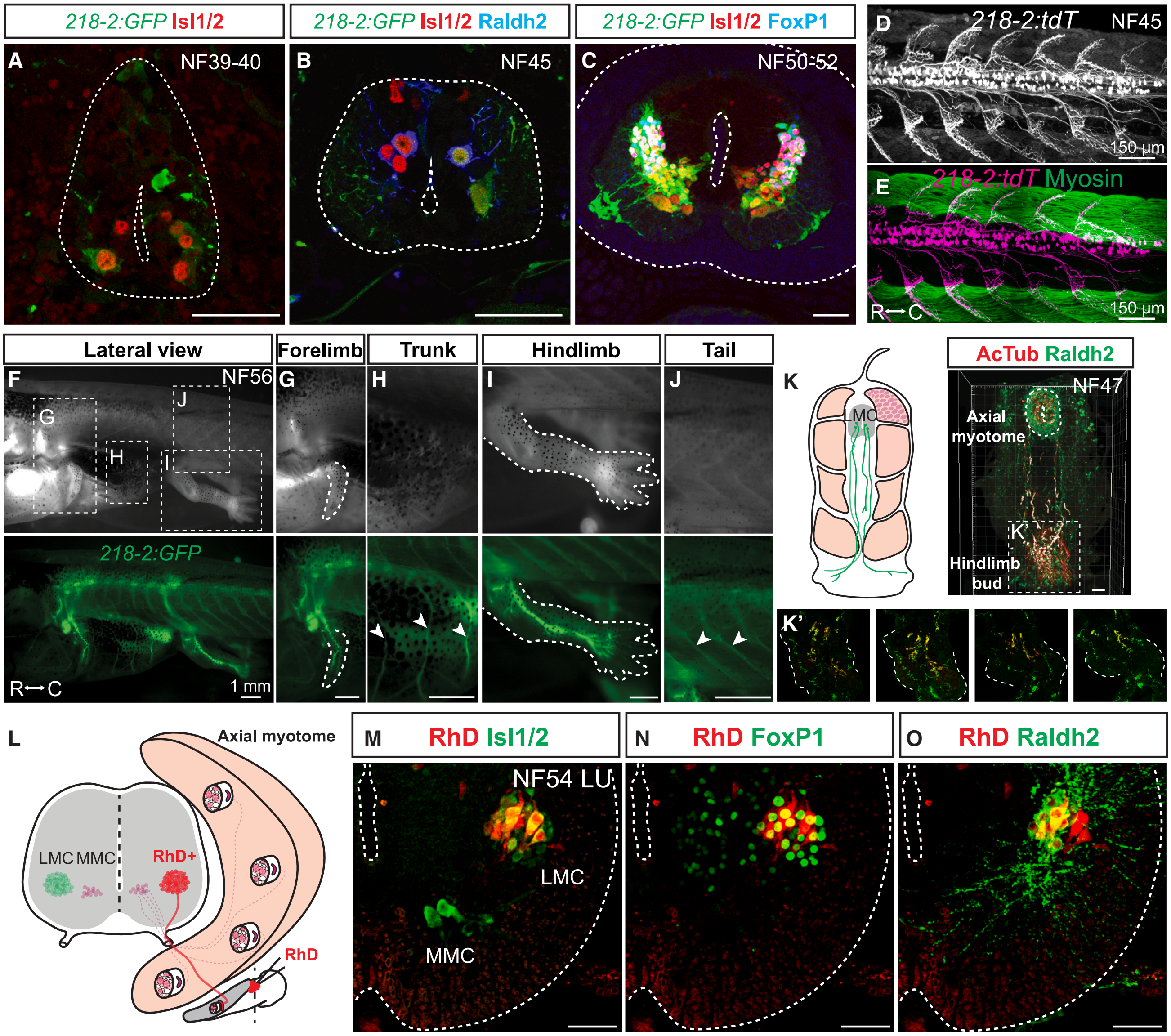

Figure 4. Linking MN molecular profiles to anatomical projection patterns during frog metamorphosis

(A–C) GFP-labeled MNs at the limb levels in *218-2:GFP* tadpoles at NF39–40 (A), NF45 (B), and NF50–52 (C) express the pan-MN marker Isl1/2 (red). At NF45 and NF50–52, a Raldh2$^+$/FoxP1$^+$ population (blue) of MNs, consistent with their LMC identity, also expresses GFP. Scale bar, 50 μm.

(D and E) MNs in free-swimming NF45 *218-2:GFP:tdT* tadpoles are distributed throughout the spinal cord and extend axonal arbors into the myotomal cleft (D), as shown by myosin heavy chain immunohistochemistry (E, green). R, rostral; C, caudal. Scale bar, 150 μm.

(F–J) GFP-labeled MNs in a limbed NF56 *218-2:GFP* tadpole (F) innervate the forelimb (G), trunk (H), hindlimb (I), or tail (J), in line with the expected innervation patterns of the molecular populations detected at this stage. Scale bar, 1 mm.

(K) A pioneering population of LMC MNs at free-swimming stage NF47 expresses the LMC marker Raldh2 (green), and their axons, marked with the acetylated-α-tubulin antibody (red), extend to the developing limb area prior to limb bud emergence (insets in K′ showing traced hindlimb bud). Scale bar, 50 μm.

(L) Schematic of medial and LMC innervation patterns and the location of the rhodamine dextran application, adapted from Lambert et al.[37]

(M–O) Retrograde labeling with rhodamine dextran (RhD, red) marks a population of laterally positioned MNs that co-express MN (M, Isl1/2, green) and LMC (N, FoxP1, green; O, Raldh2, green) markers. Scale bar, 50 μm.

MN identity delineates projection patterns across frog metamorphosis

To investigate how the metamorphic addition of muscles and transcriptionally distinct MN subtypes is reflected in MN anatomy and connectivity, we generated two MN-specific transgenic lines, *Xla.Tg(218-2:GFP)*^{Swee} and *Xla.Tg(218-2:tdTomato)*^{Swee}, using the murine microRNA-218 enhancer.[63] Throughout frog development and consistent with expression in mice, *218-2*-driven fluorophores were selectively expressed in MNs, marked by Isl1/2 and column-specific TFs (Figures 4A–4C). This allowed us to visualize the progressive emergence of MN projections during metamorphosis (Figures 4D–4J).

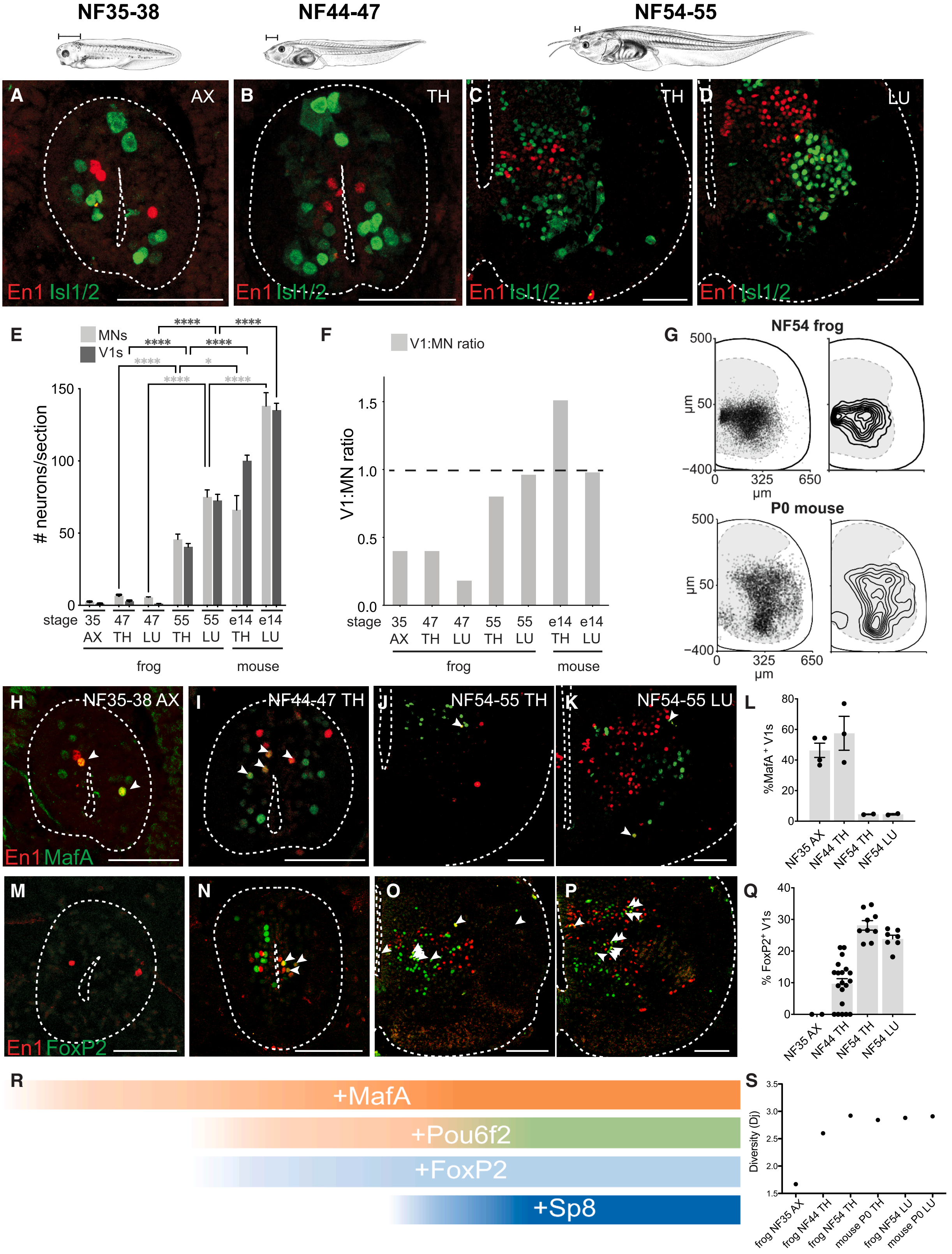

(legend on next page)

At free-swimming stages, the *218-2*$^+$ MN projections in the tail exhibited a stereotyped projection pattern consistent with their MMC identity, forming repeated, symmetrical arborizations within the myotomal cleft of the body wall musculature (Figures 4D and 4E). With limb development, additional *218-2*$^+$ axons projected from the brachial and lumbar enlargements to the fore- and hindlimb, respectively (Figures 4G and 4I). Remarkably, this MN-to-limb connectivity was already established by pioneering LMC neurons at free-swimming stages, before visible limb growth (Figure 4K). Both early and late populations of limb-innervating MNs expressed the LMC markers Raldh2 and FoxP1 (Figures 4B and 4C), consistent with those in mice[56] and confirming their LMC identity. Innervation of the trunk and tail was also observed during metamorphosis, reflecting the expansion of HMC and PGC or MMC motor columns, respectively (Figure 4H).

To complement transgenic labeling, we used retrograde dye tracing to selectively mark limb-projecting MNs, as previously described.[37] This approach further aligned molecular identity with anatomical connectivity in emergent limb MNs (Figures 4L–4O). Together, these data demonstrate the conservation of MN molecular and anatomical identity across species and the progressive diversification of MN subtypes during frog metamorphosis.

V1 inhibitory neurons increase 70-fold in number during swim-to-limb circuit transformation

The expansion and diversification of MNs during metamorphosis raised the question of whether spinal interneurons, the core regulators of locomotor patterns,[1,4,43] also changed with the emergence of limb-based locomotion. Our single-cell analysis demonstrated that all ventral cardinal classes were present throughout metamorphosis but that the V1 inhibitory population had the largest proportional increase. In mice, V1s influence locomotor speed[64–66] and flexor-extensor alternation[19,67,68] — both emergent features of the metamorphic transition (Figure 1). This motivated us to evaluate V1 interneuron number *in situ* across the tail-to-limb transition in frogs.

At all stages, we identified neurons in the spinal cord expressing the well-established V1 marker En1[44,45] (Figures 5A–5D). This V1 neuron population expanded with increasing movement complexity, with ~1 V1 per 15 μm hemi-section at larval swim stages (Figures 5A and 5E), ~2.5 at free swim stages (Figures 5B and 5E), and ~40 in thoracic and ~70 in lumbar at the peak of limb circuit development (Figures 5C, 5E, S4C, S4D, and S4H–S4K). During metamorphosis, V1 interneurons thus increased ~70-fold (Figures 5C–5E) with the emergence of MN diversity and circuits for limb movement.

This expansion led us to evaluate how the ratio between V1s and MNs, a numerical proxy for interneuron regulation of motor output, varied across metamorphosis. The V1:MN ratio increased from 0.5:1 to 1:1 with the transition from swim to limb circuits (Figure 5F). This 1:1 V1:MN ratio mirrored that of mice at comparable developmental stages[9,11,51,69] and is thus a conserved feature of developing tetrapod limb circuits. We additionally compared the settling position of V1s between frogs and mice, as previous reports correlate settling position with functional properties.[9,12,67] As in mice,[9,19,69] the V1 population in frogs spanned nearly the entire ventral horn of the spinal cord and peaked in its distribution in the middle of the mediolateral axis (Figures 5G and S7A–S7C). Together, these data demonstrate scaling of V1 inhibitory neurons to MNs with increased complexity of motor output, culminating in highly conserved limb motor circuits across species.

Stepwise emergence of extensive inhibitory cell type diversity during metamorphosis

The increase in V1 number during the swim-to-limb transition led us to hypothesize that the addition of interneuron subtypes may underlie the metamorphic complexification of frog movement. In mammals, V1 interneurons are subdivided by TF expression into clades and subtypes with differing molecular profiles, settling positions, projection patterns, and electrophysiological properties.[9,11,12,17,70–73] They include the physiologically defined Renshaw cells for recurrent inhibition,[67,74,75] Ia-inhibitory neurons for reciprocal inhibition,[67] and numerous other molecularly distinct cell types[9,11,12,17] of unknown function. In larval tadpoles, electrophysiological analysis has shown that V1 inhibitory interneurons are present and active during swimming,[76] but their molecular cell type composition at larval and later limb circuit stages is unknown. We thus examined V1 heterogeneity across metamorphosis to determine whether high levels of subtype heterogeneity represent a specialization for mammalian movement

Figure 5. V1 inhibitory INs increase in number and diversity with metamorphic expansion of MNs

(A–D) Immunoreactivity against Engrailed-1 (En1, red), a V1 inhibitory IN (V1) marker, and Isl1/2 (green), a MN marker, labels ~1 V1 and ~2.5 MNs at NF35–38 (A), ~2 V1s and ~5.5 MNs at the TH levels at NF44–47 (B), and at NF54-55, ~40 V1s and ~45 MNs at the TH levels (C) and ~72 V1s and ~75 MNs at the LU levels (D).
(E and F) Number (E) and ratio (F) of V1s and MNs at AX (NF35) and TH and LU (NF47 and NF55 tadpole and E14 mouse) levels. At NF35 and NF47, the V1:MN ratio is under 0.5 and then approaches 1 at NF54–55 for both TH and LU segments in metamorphosing frogs, similar to in the embryonic mouse. Shown in (E) is the mean ± SEM for 4–17 animals per 15 μm ventral horn. Two-way ANOVA with Šídák multiple comparisons test was used for (E). $^*p < 0.05$, $^{****}p < 0.0001$.
(G) Position of V1 INs at LU levels of NF54 frog (top) and P0 mouse (bottom). Plotted on the left are individual cells with 50% transparent black to highlight overlap.
(H–R) V1 clades emerge sequentially during the *Xenopus* swim-to-limb transition. At larval swim stages, V1s lack diversity: ~50%–60% marked by MafA (H) and MafB (Figure S8); FoxP2 (M), Pou6f2, and Sp8 are absent (Figure S8). At free-swimming NF44–47 stages, alongside the MafA population (I), the FoxP2 (N) and Pou6f2 (Figure S8) clades emerge. During metamorphosis, V1s acquire the four-clade organization observed in the mouse, with maintenance of MafA (J and K), expansion of the FoxP2 (O and P), and emergence of the Sp8 population (Figure S8). Percentage of V1 INs expressing clade markers MafA (L) and FoxP2 (Q) in AX (NF35–38), TH (NF44–47 and NF54–55), or LU spinal cord (NF54) (mean ± SEM, n = 4–10 animals). Schematic sequence of V1 clade emergence (R): MafA is present in escape swimming; MafA, Pou6f2, and FoxP2 in free-swimming; and all four clades at limb-circuit stages. Arrowheads indicate coexpression.
(S) Entropy analysis of "diversity" index based on TF expression shows a significant increase in overall transcriptional diversity between NF35 and NF44 and a peak of diversity reached at NF54–55. The diversity at the peak matches that of the neonate mouse.
Shown is either a spinal cord cross-section (NF35–38/44–47) or a ventral hemi-section (NF54–55) with the central canal and outer edge indicated (dotted line). Scale bar in micrographs, 50 μm and in drawings, 1 mm. Tadpole drawings adapted from *Xenopus* illustrations © Natalya Zahn (2022).[29]

or a conserved trait across vertebrates and how V1 diversity may scale with the swim-to-limb transition.

To address this, we focused our first analysis on the transition from larval swim to free swim to limb stages. We profiled four V1 clade markers—MafA, Pou6f2, FoxP2, and Sp8 (Figures 5H–5Q and S8A–S8D)—and an additional five TFs that subdivide V1 interneurons in mice[9] (Figures S8A–S8D). Larval tadpole V1s were largely homogeneous, co-expressing the MafA clade marker and MafB (Figures 5H, 5L, S8A, S8D, and S8E). With the emergence of free swimming,[26] hypaxial musculature,[77] and dorsal root ganglia,[78] V1 transcriptional heterogeneity increased, with Pou6f2 and FoxP2 clades added (Figures 5N, 5Q, S8B, S8D, and S8F). Then, with limb circuit addition, all clade and subtype markers were expressed (Figures 5J–5L, 5O–5Q, S8C, S8D, S8G, and S8H). As in mice,[12] the first clade to emerge was MafA, followed by Pou6f2, FoxP2, and Sp8 (Figure 5R), indicating high conservation of the timing of V1 interneuron development between species.

To quantify this increasing transcriptional diversity across metamorphosis, we calculated the transcriptional entropy[79] at each stage using information theory and fractional TF expression (STAR Methods). Entropy initially increased between larval and free swimming stages and again rose with the development of limb circuits, resulting in comparable high V1 diversity between frogs and mice (Figure 5S). Our analysis thus demonstrates that V1 interneurons are added and sequentially diversify into numerous transcriptionally distinct subpopulations as tadpoles transition to frogs.

Combinatorial TF patterns reveal conserved and divergent inhibitory populations across limbed vertebrates

The emergence of V1 clades and transcriptional diversity with the addition of limbs motivated us to evaluate the extent to which V1 transcriptional features are shared or divergent between limb circuits across species. In mice, several rules define V1 transcriptional heterogeneity at limb levels[9–11]: (1) V1 clades are non-overlapping and differ in size and position, (2) additional TFs mark positionally and functionally distinct V1 subsets,[12,68,75] and (3) TF combinations further carve out extensive V1 heterogeneity.[9–11] To test whether these principles apply to *Xenopus* frogs, a species with a simplified repertoire of limb movements compared to mice,[3] we profiled the combinatorial TF expression of lumbar V1s at the peak of their differentiation: NF54–55 in frogs (Figures S4C, S4D, and S4H–S4K) and post-natal day 0 (P0) in mice.[9]

Remarkably, while the hallmark features of mouse V1 interneurons were largely recapitulated in frogs, notable species-specific differences also emerged. The four V1 clade markers were mutually exclusive in their expression, defining V1 subpopulations of similar proportion and spatial organization as in mice (Figures 6A–6D). This cross-species similarity extended to ten TFs that diversify mouse V1s (Figure 6D and S9G–S9Q), including MafB, which, in combination with Calbindin, constitutes the molecular signature of functionally distinct Renshaw cells.[67,75]

Further analysis of two-TF ($V1^{2TF}$) and three-TF ($V1^{3TF}$) combinations in frogs delineated numerous molecularly distinct subpopulations, mirroring those in mice.[9,11] For many $V1^{2TF}$ subpopulations, the co-expression rules established in mice were largely upheld in frogs (Figure 6E). However, among these subpopulations, species-specific patterns emerged: six $V1^{2TF}$ and nine $V1^{3TF}$ subsets were selectively enriched in one species; of these, 11 were mouse and 4 were frog enriched (Figure 6E). Notably, FoxP1/2/4 and Otp combinatorial expression marked several mouse-enriched populations, while Sp8 in combination with Otp defined the most frog-enriched population (Figure 6E). Combinatorial TF expression thus reveals fine-scale interspecies differences in spinal interneurons, constituting a potential substrate for differences in motor output.

In mice, one critical aspect of V1 diversity is its variation between limb and torso levels,[11,71] aligning with variant functional properties of limb-related versus autonomic and torso-associated motor output.[80] This motivated us to extend our analysis to the thoracic spinal cord. As in mice,[11,51,56,71] thoracic circuits were downscaled in frogs, with half the number of MNs and V1 interneurons as limb circuits (Figures S9A–S9D). This conservation of thoracic circuit properties across species extended to the V1 clades and $V1^{1TF}$ subpopulations (Figure S9E–S9Q). Similarly, thoracic-enriched subpopulations identified in mice were also thoracic enriched in frogs (Figures 6F–6I). However, at thoracic levels as at limb levels, further combinations of two- or three-TFs defined species-specific subpopulations, selectively enriched in either mouse or frog (Figure S9F).

This striking similarity of V1 transcriptional properties across spinal cord levels and between distant vertebrate species demonstrated conservation of four-limbed vertebrate interneuron architecture. However, within this conserved framework, species-specific divergence arose at all spinal cord levels via fine-scale subpopulations defined by higher-order TF combinations.

FoxP1 determines limb MN identity and function during metamorphosis

Our cell type analysis revealed a multifold scaling of spinal circuit complexity during frog metamorphosis, culminating in highly diverse neuron types similar to those in mice. However, the functional significance of this high molecular heterogeneity remains unclear across species. While inactivation or ablation of entire classes of spinal neurons has been shown to cause motor deficits in mice and zebrafish,[1,6] still unclear are the specific contributions of individual subpopulations to movement and how the TFs that define this diversity may differentiate their connectivity and function.

We therefore used CRISPR-Cas9 gene editing to perturb TFs that mark MN and V1 cell types and to evaluate their function in generating cell type diversity and locomotor output across swim and limb stages. In mice, limb MN identity is specified by the TF FoxP1, and its loss disrupts the coordination of limb movement.[56,81,82] To evaluate the specificity of FoxP1 function in limb versus swim circuits and to assess its evolutionary conservation in specifying MN identity across vertebrates, we generated both unilateral and bilateral FoxP1 CRISPR mutant animals using established methods[83] (Figures 7A, 7B, S10A, and S10B). Bilateral mutants first developed normally (Figure S11J) but then exhibited defective limb posture and died at juvenile frog stages, mirroring the lethality observed at

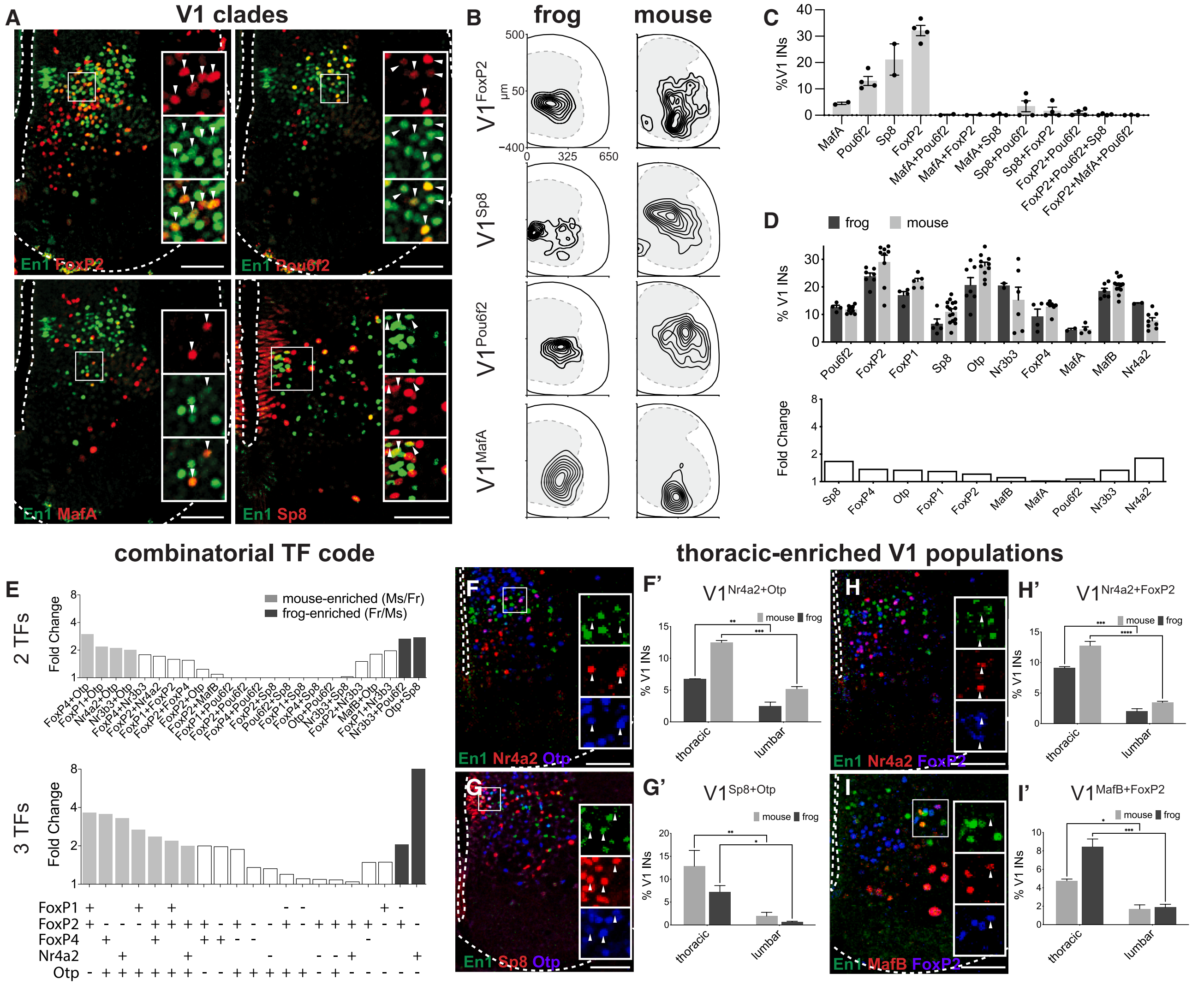

Figure 6. Conservation of V1 clade organization and transcriptional diversity between frog and mouse

(A) Mouse V1 clades are conserved in the frog. Antibodies against FoxP2, Pou6f2, MafA, and Sp8 TFs (green) label subsets of $En1^+$ V1 INs (red) in LU spinal cord of NF54–55 tadpoles. Shown is a ventral hemi-section of spinal cord with the central canal and outer edge indicated (dotted line). Scale bar, 50 µm.

(B) Spatial distribution plots of $V1^{FoxP2}$, $V1^{Sp8}$, $V1^{Pou6f2}$, and $V1^{MafA}$ at the LU level in NF54–55 tadpole (left) and P0 mouse (right). Frog and mouse V1 clades have similar settling positions. Frog spinal cords were resized to mouse-like proportions (STAR Methods). Plotted are INs from at least 20 LU spinal cord hemi-sections from at least 2 animals.

(C) Frog V1 clades are mutually exclusive in their expression. The bar plot shows the percentage of V1s expressing a singular or combination of clade markers FoxP2, Sp8, Pou6f2, and MafA. Shown is mean ± SEM, $n = 2–4$ animals.

(D) V1 molecular subsets are present in similar proportions in the frog and mouse. Top: bar plot showing the percentages of V1s expressing a given TF in LU NF54–55 tadpole (black) and P0 mouse (gray) spinal cords determined by immunohistochemistry. Bottom: bar plot showing the fold change in percentage of V1 subsets between the frog and mouse; no change larger than 2-fold was observed. Shown is mean ± SEM (2TF: $n = 2–6$ animals; 3TF: $n = 2$ animals). Kruskal-Wallis test with Dunn's multiple comparisons test was used for (D) (top).

(E) V1 INs marked by two and three TFs reveal species-enriched subsets. Shown is fold enrichment of $V1^{2TF}$ and $V1^{3TF}$ INs with >2-fold enrichment in NF54–55 frog (black) or P0 mouse (gray) spinal cord.

(F–I) Mouse TH-enriched populations of V1 are present and enriched at the TH levels in frog. $V1^{Nr4a2+Otp}$, $V1^{Sp8+Otp}$, $V1^{Nr4a2+FoxP2}$, and $V1^{MafB+FoxP2}$ populations are present in the frog (gray) TH spinal cord (left) and significantly enriched compared to the LU level (right). The same rostocaudal enrichment was reported in the mouse (black). Shown is mean ± SEM for 2–6 animals with significant differences ($p < 0.05$) plotted. Two-way ANOVA with Šídák multiple comparisons test was used for (F′) and (H′) and uncorrected Fisher's Least Significant Difference for (G′) and (I′). $^*p < 0.05$, $^{**}p < 0.01$, $^{***}p < 0.001$, $^{****}p < 0.0001$. Scale bar, 50 µm.

birth in FoxP1 mutant mice.[56] Unilateral mutants, however, were largely unaffected in their morphology, displaying only abnormal limb posture on the mutant side (Figure 7F).

Genetic and immunohistochemical analysis confirmed efficient and specific FoxP1 loss with an ~80% reduction in $FoxP1^+$ MNs (Figures 7B, 7C, S10B, S10C, S10E, and S10F).

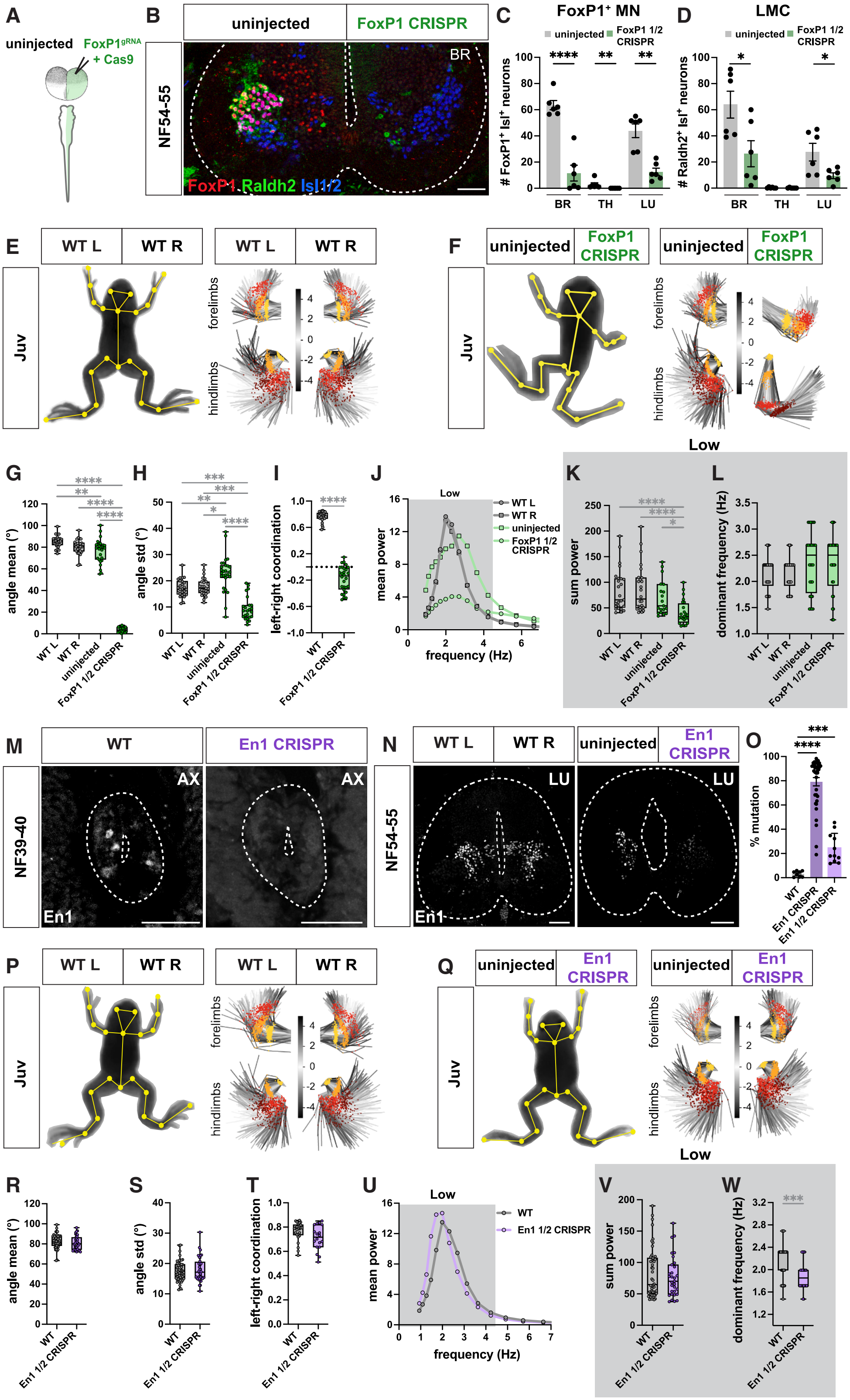

(legend on next page)

This loss of FoxP1 caused a near-complete transformation of limb MN identity, as indicated by a ~70% reduction in MNs expressing Raldh2, an independent LMC marker[60] (Figures 7B, 7D, S10B, and S10D). In contrast, the number of MMC MNs, V1 inhibitory neurons, and 12 V1 subtypes, with the exception of $V1^{FoxP1}$, $V1^{FoxP2}$, and $V1^{FoxP2+Otp}$, were unaffected (Figures S10G–S10J). In addition, analysis of MN axon projections revealed that innervation of the limb was maintained despite the disrupted LMC identity (Figures S10K and S10L), paralleling similar observations in mice.[56]

Frog metamorphosis uniquely positioned us to assess FoxP1's role in both limb- and swim-driven locomotion. We evaluated motor behavior of unilateral and bilateral FoxP1 CRISPR mutant frogs and tadpoles, respectively. Mutant frogs exhibited a unilateral loss of fore- and hindlimb movement with a defective posture and range and a loss of power, but not frequency, of limb movement on the mutant side (Figures 7E–7H, 7J–7L, S11G, and S11I). This loss resulted in a reduction in left-right coordination of the hindlimb (Figures 7I and S11H); a corresponding increase in the amount of turning, likely due to the asymmetry of limb propulsion (Figure S11F); and an overall decrease in the animal's acceleration, distance and time spent moving (Figure S11A–S11E; Video S8). Free-swimming tadpoles however showed no defects in these parameters, and their tail range was unaffected (Figure S11J–S11P).

Together, these cellular and behavioral results underscore a remarkable conservation of FoxP1-dependent limb MN specification and function between frogs and mice.[82] FoxP1 thus emerges as a transcriptional regulator of limb circuits across distant species, selectively defining limb motor output.

Differential function of En1 in tadpole swim versus frog limb motor output

V1 inhibitory neurons are critical regulators of motor output, as they synapse onto MNs and modulate their firing patterns to generate movement.[9,12,43,84,85] As we demonstrate, the heterogeneity of V1 cell types is one of the defining features of limb circuits across species. This striking heterogeneity raises the question of what drives V1 diversity and how this diversity may differentiate motor function. As frog metamorphosis uniquely captures the expansion and diversification of V1 inhibitory circuits, it empowers us to dissect V1 heterogeneity and function. An attractive but still poorly understood candidate TF for driving V1 diversity is En1, as it is expressed during the differentiation of the V1 class,[69] but its role in subtype specification and locomotor output is poorly understood.

Figure 7. CRISPR loss of function of FoxP1 and En1 causes selective loss of the range/coordination or frequency of limb movement in *Xenopus* frogs, respectively

(A and B) Generation of unilateral FoxP1 CRISPR mutant frogs by injection of FoxP1 single guide RNA (sgRNA) and Cas9 protein in a single cell at the two-cell stage (A) results in NF54–55 tadpoles in which FoxP1 (red) and Raldh2 (green) immunoreactivity is selectively absent from the mutant side of the spinal cord (B). $Isl1/2^+$ (blue, marker for MNs in the ventral spinal cord) neurons are present on the wild-type and mutant side of the spinal cord (B). Dashed lines indicate the central canal and spinal cord boundaries; scale bar, 50 μm.

(C and D) Cell type characterization in unilateral FoxP1 CRISPR mutant animals. Quantification of spinal cord cell numbers at BR, TH, and LU reveals loss of $FoxP1^+$ $Isl1^+$ neurons at all levels (C) and loss of $Raldh2^+$ $Isl1^+$ neurons at BR and LU levels (D). $n = 6$ for WT, $n = 6$ unilateral FoxP1 CRISPR. Unpaired t test was used for (C) (BR) and (D) (BR and LU). Mann-Whitney test was used for (C) (TH and LU) and (D) (TH). $^*p < 0.05$, $^{**}p < 0.01$, $^{****}p < 0.0001$.

(E–I) Loss of range and coordination of movement of the FoxP1 mutant hindlimb. Wild-type (WT) (E) and unilateral FoxP1 CRISPR (F) juvenile frogs with SLEAP skeleton (left, yellow) superimposed on animal image. PCA plots represent the position of the fore- and hindlimbs and their range of movement during 256 random frames and show a different position and range of the FoxP1 CRISPR limbs compared to the WT or the uninjected side (E and F, right; hip and shoulder, yellow; knee and elbow, orange; ankle and wrist, red; foot, brown). Scale bars in (E) and (F) indicate the color code of the first principal component of variation of the aligned fore and hindlimb positions. The FoxP1 CRISPR mutant knee also differs in its mean angle (G), and its movement range is reduced (I). In contrast, the uninjected side displays a higher range of movement (H). Left-right coordination between knee joints is lost in FoxP1 CRISPR animals (I; +1 = bilateral synchronous, 0 = random, −1 = alternate synchronous). $n = 13$ for WT, $n = 14$ for unilateral FoxP1 CRISPR. Brown-Forsythe and Welch ANOVA tests were used for (G). Kruskal-Wallis test was used for (H). Mann-Whitney test was used for (I). $^*p < 0.05$, $^{**}p < 0.01$, $^{***}p < 0.001$, $^{****}p < 0.0001$.

(J–L) FoxP1 CRISPR mutant hindlimbs maintain dominant frequency but lose power. Mean power spectrum of knee oscillations shows only one peak in the low frequency range for WT, uninjected, and FoxP1 CRISPR hindlimbs (J; 0.9–4.5 Hz, dark gray). At the knee joint, the amount of movement in the low-frequency bin (0.9–4.5 Hz), represented by the sum power, is lower on the mutant side compared to the uninjected side and WT (K). Dominant frequency is unaffected on uninjected and FoxP1 CRISPR sides (L). $n = 13$ for WT, $n = 14$ for unilateral FoxP1 CRISPR. Kruskal-Wallis test was used for (K) and (L). $^*p < 0.05$, $^{****}p < 0.0001$.

(M–O) Characterization of En1 CRISPR mutant animals. En1 sgRNA and Cas9 protein were injected at the one-cell stage to generate bilateral mutant animals, resulting in loss of En1 immunoreactivity from both sides of the spinal cord at NF39–40 (M, right, white) or at the one-cell and two-cell stage to generate unilateral mutant animals with loss of En1 immunoreactivity only from the En1 CRISPR side of the spinal cord at NF54–55 (N, right, white). TIDE analysis reveals high efficiency of En1 sgRNA in generating NF44–48 bilateral and ~25% mutation rate for juvenile unilateral CRISPR animals (O; $n = 8$ for WT, $n = 36$ for En1 bilateral mutants, $n = 8$ for En1 unilateral mutants). For unilateral mutants, the precision of TIDE analysis did not allow prospective identification of the mutant side, and thus data from injected and uninjected sides were pooled (O–W). Dashed lines indicate the central canal and spinal cord boundaries; scale bar, 50 μm. Mann-Whitney test was used for (O) (WT versus En 1/2 CRISPR), and unpaired t test was used for (O) (WT versus En1 CRISPR). $^{***}p < 0.001$, $^{****}p < 0.0001$.

(P–T) Range and coordination of movement are unaffected in juvenile unilateral En1 CRISPR mutant animals. WT (P) and unilateral En1 CRISPR (Q) juvenile frogs with SLEAP skeleton (yellow) superimposed on animal image. PCA plots represent the position of the fore- and hindlimbs and their range of movement during 256 random frames and show no visible difference in range between WT, uninjected, and En1 CRISPR sides (P and Q, right; hip and shoulder, yellow; knee and elbow, orange; ankle and wrist, red; foot, brown). Scale bars in (P) and (Q) indicate the color code of the first principal component of variation of the aligned fore- and hindlimb positions. Unilateral En1 CRISPR mutant knees show a similar mean angle (R) and angle range (S) as the WT. Left-right coordination between knee joints is also unaffected in unilateral En1 CRISPR animals, as their pattern of movement resembles the bilateral synchronicity of WT (T; +1 = bilateral synchronous, 0 = random, −1 = alternate synchronous). $n = 13$ for WT, $n = 8$ for unilateral En1 CRISPR. Welch's t test was used for (R) and (S); Mann-Whitney test was used for (T).

(U–W) Lower dominant frequency in juvenile En1 CRISPR mutant hindlimbs. Mean power spectrum of the knee oscillation shows only one peak in the low-frequency bin (0.9–4.5 Hz, dark gray) for WT and unilateral En1 CRISPR animals (U). At the knee joints, the amount of movement, represented by the sum of the power, is similar between WT and unilateral En1 CRISPR animals (V). However, the dominant frequency of the knees is lower in unilateral En1 CRISPR animals compared to the WT (W). $n = 13$ for WT, $n = 8$ for unilateral En1 CRISPR. Mann-Whitney test was used for (V) and (W). $^{***}p < 0.001$.

To address these questions, and more specifically, to define how En1 affects swim versus limb movement, we generated bilateral and unilateral En1 CRISPR mutant animals with corresponding high-efficiency mutation and En1 protein loss (Figures 7M–7O). We first evaluated how En1 loss of function affected tail movement in free-swimming tadpoles, a time point when V1 inhibitory neurons exhibit intermediate levels of subtype diversity (Figure 5S). Bilateral mutant tadpoles moved less overall, shifted to low-frequency tail oscillations, and exhibited an additional reduction of the dominant low frequency (Figures S12A–S12E and S12H–S12L). They also showed an increase in turning and a larger range of tail movement (Figures S12A, S12F, and S12G). Taken together, these results revealed a conserved role of En1 in determining tail frequency in tadpoles, mirroring frequency defects in V1-deficient zebrafish,[66] and an emergent role in specifying the range of tail movement during swimming.

We next evaluated the role of En1 in the specification and function of limb circuits in frogs. As bilateral En1 CRISPR mutants die before metamorphosis,[86] we analyzed unilateral mutant frogs, which developed normally and exhibited no gross movement impairments (Figures 7P, 7Q, and S12M–S12R; Video S9). Kinematic analysis revealed that loss of En1 selectively decreased the dominant frequency of hindlimb movement at all joints while leaving its power, range, and left-right coordination unaffected (Figures 7R–7W and S12S–S12W). This specificity of the En1 phenotype for frequency modulation in frog limb circuits matches concurrent findings in mice[20] and establishes the En1 TF as a selective determinant of limb movement frequency, but not range, across species.

Such selective loss of frequency at limb stages in En1 CRISPR mutant animals motivated us to examine how En1 shapes the subtype architecture of spinal interneurons. We first evaluated specificity at the level of cardinal class: finding a reduction of En1-expressing V1 interneurons in En1 CRISPR mutant as compared to uninjected control animals but equivalent numbers of cells expressing the dI6 marker Dmrt3[87] and the V2a marker Chx10/Vsx2[88] (Figures S13A–S13C and S13H). Despite this selective loss of En1 protein, however, the four primary V1 clade markers Pou6f2, Sp8, FoxP2, and MafA were unaffected (Figures S13D–S13H). This loss of En1 protein precluded us from further evaluating V1 diversity using immunohistochemistry. Thus, to characterize subtype diversity, we instead utilized multiplexed *in situ* hybridization chain reaction (HCR) analysis (STAR Methods). *Foxd3*, an independent marker of V1 inhibitory neurons,[71,75] was maintained in both wild-type and En1 mutant animals (Figure S13I–S13R and S13T), indicating that V1s still developed in the absence of En1 (Figure S13S) and giving us a secondary method to identify them and evaluate V1 subtype diversity (Figure S13U). Paralleling observations in mice,[9] in wild-type frogs, *nr5a2* marked a subset of V1 interneurons; in En1 CRISPR mutants, however, this *nr5a2*-expressing subset was reduced in number (Figures S13I, S13J, S13V, and S13V′). This contrasted with other clade V1 subset markers (*pou6f2*, *foxp2*, *sp8*, and *mafa*) that were unaffected (Figure S13K–S13R and S13W–S13Z′). Together, these data indicate that loss of En1 selectively affects *nr5a2*-expressing V1s and disrupts limb frequency control. Across limbed species, these results support a model where V1 function segregates by subtype, with the V1 population as a whole controlling both frequency and flexion/extension[19,65,68] and the V1-determined *nr5a2* subset only the frequency of limb locomotion.

Collectively, our analysis of frog metamorphosis illuminates differential functions of En1 across swim versus limb stages. In tadpole swim circuits that exhibit low V1 diversity, En1 functions as a general regulator of both range and frequency of movement, specifying multiple functions with a limited number of cell types. In contrast, in frog limb circuits characterized by high V1 diversity, En1 specifies individual V1 subtypes dedicated to frequency control. One TF can therefore differentiate the function of inhibitory circuits in tail versus limb motor control via regulation of molecularly defined subpopulations.

DISCUSSION

Understanding how neural circuits are organized to implement movements of varying levels of complexity is a fundamental goal of neuroscience. Our cellular and behavioral analysis of spinal circuits during frog metamorphosis demonstrates that the number and diversity of motor and inhibitory neurons increase dramatically as tadpoles transition from tail-based swimming to four-limbed locomotion. Expanded arrays of transcriptionally diverse V1 inhibitory neurons in particular emerge as critical building blocks of limb motor control. Frog metamorphosis thus exemplifies how motor circuits scale in their cell type complexity to accommodate increasing sophistication of behavior.

Molecular and cellular mechanisms of motor circuit expansion and diversification

Simple rewiring of existing swim neurons or addition of the same cell types is not sufficient for an increased limb motor repertoire. Instead, our data show the generation and incorporation of neuron types. The magnitude of this change is the most striking for V1 inhibitory neurons, with an ∼70-fold increase in number and addition of numerous, combinatorially defined molecular subtypes.

Multiple mechanisms could drive this expansion and diversification. We identify transcriptional programs activated during metamorphosis that orchestrate spinal neuron diversification, mimicking classical master regulators in other species.[89] We strengthen the species ubiquity of FoxP1 as a determinant of limb MN identity and identify En1 as a specifier of V1 diversity in limb circuits, aligning with parallel findings in mice.[20] Our data thus reaffirm the importance of intrinsic and hierarchical transcriptional regulation of emergent circuitry.

The timing of motor circuit expansion and diversification, however, aligns precisely with limb development, raising the possibility that the limb itself triggers spinal neuron heterogeneity. We show that loss of MN diversity does not affect inhibitory neuron diversity, echoing previous studies that refute interdependence between MN and interneuron specification.[11] However, the contribution of other limb- or sensory neuron-derived signals in driving spinal neuron heterogeneity remains to be determined. Notably, in chicks, complete ablation of the limb results in a selective loss of motor pool diversity.[90]

Alternatively, a systemic trigger of this expansion could be thyroid hormone, which mediates metamorphic progression[28,91,92] as well as neuronal maturation and cell type specification in the brain.[93] Consistent with this, ectopic application of thyroid hormone in tadpoles induces premature neuron heterogeneity in the spinal cord (data not shown). Frog metamorphosis thus provides an inroad to mechanistically link hormone signaling to transcriptional diversity in the spinal cord.

Addition of limb to existing swim circuits

The tadpole-to-frog transition also exemplifies more generally how movement patterns and the circuits that underlie them can emerge, disappear, and change during an organism's development. To execute the switch between tail and limb motor patterns, additional neurons must be integrated into existing swim circuits. In invertebrates, pre-existing circuits can facilitate the incorporation of emergent circuits.[94–96] Similarly, in frogs, we find that pioneering neurons innervate the nascent limb bud at swim stages, positioning them as an anatomical scaffold for later-developing limb circuits.

This coexistence of emergent and existing circuits also seems to instruct their function. At intermediate stages of metamorphosis, emerging or receding circuits are rhythmically coupled to existing ones. Such coupling of emergent to existing or receding to remaining circuits provides a generalizable mechanism for the remodeling of behavior via neuron- and circuit-level interactions.

Evolution of vertebrate spinal cord cell types for swim versus limb movement

Our study of amphibians not only informs these fundamental questions of development and remodeling but also those of motor circuit origins and evolution. As the first vertebrates to emerge with limbs, amphibians occupy a unique position on the phylogenetic tree between aquatic and terrestrial species.[97] Frogs, like many other amphibians, also recapitulate this evolutionary transition in their own development.[23]

We find a conserved substrate of swim and limb movement that consists of all 12 cardinal classes of spinal neurons. Within this conserved core, limb control additionally requires selective amplification of inhibitory neuron number and transcriptionally distinct cell types. Our observations during metamorphosis predict the core components and circuit-level modifications that may have underlain the comparable aquatic-to-terrestrial transition during vertebrate evolution.

From a comparative perspective, aquatic behavior takes many forms; lampreys swim with rhythmic body oscillations, zebrafish in defined bouts with varying speeds, and tadpoles in spiral trajectories and then constant, directed movement. Such basic swim movement patterns, as we demonstrate in tadpoles, require a baseline of neuron cell type specialization. In larval *Xenopus*, we find that swimming is generated by only one column of axial MNs, as in lampreys[98] and larval zebrafish,[99] and one clade of V1 interneurons. This uniformity of larval tadpole circuits is corroborated by their homogeneous electrophysiological properties[76] and predicts that other organisms with simple axial-based escape swimming may similarly lack V1 diversity.

As compared to larval swimming, free swimming in tadpoles is characterized by increased locomotor complexity and more V1 inhibitory neuron types. This aligns with recent studies showing that zebrafish interneurons exhibit diversity in their anatomy and electrophysiology.[7,8] In zebrafish, which have exceptionally high-speed movement, motor and interneurons have co-evolved into slow, intermediate, and fast subpopulations.[8] In *Xenopus* tadpoles, which move at lower frequencies, such sub-specialization has not yet been found.[100] Therefore, a molecularly and physiologically homogeneous set of motor and interneurons may have originated in an aquatic ancestor of vertebrates, with additional cell types evolving later for specialized motor programs.

Frogs also provide the unique opportunity to evaluate the emergence and conservation of limb behavior. Their metamorphic transformation from tail to limb movement necessitates the recruitment of additional muscles and MNs. As in mice, we show that *Xenopus* MNs segregate into columns, divisions, and pools, with FoxP1 serving as an evolutionarily conserved specifier of LMC MN fate. Shared strategies are thus employed to establish the building blocks of motor circuits even though their output differs. These blocks are remarkably conserved between amphibians and mammals and may extend even further in vertebrate evolution.[58,101]

The similarity of MNs across distant vertebrates but varied motor output raises the question of whether spinal interneurons are also conserved. Here, we demonstrate that nearly the same transcriptional logic subdivides inhibitory interneurons across distant limbed species. We also find, however, that higher-order distinct combinatorial TF codes define species-specific divergence. This high degree of spinal interneuron heterogeneity is thus not an exclusive feature of murine or mammalian motor circuits and was likely acquired as a common limb locomotor adaptation during the evolutionary water-to-land transition.

Intriguingly, we also show that the TF En1 regulates the frequency, but not the range, of movement in frogs, which coincides with concurrent observations in mice.[20] Strikingly, limb locomotion in frogs and mice exhibits nearly the same frequency.[33] Such potent conservation of gene-to-function relationships between amphibian and mammalian limb circuits also extends further to swim circuits, as En1 loss in tadpoles, like V1 ablation in zebrafish,[66] disrupts tail frequency. Common behavioral features can therefore be linked to highly conserved transcriptional programs and cell types.

Linking cell types to divergent motor behavior strategies across species

In addition to identifying conserved mechanisms of motor output regulation, our study also sheds light on cellular and circuit mechanisms underlying divergent motor output. In tadpoles, unlike zebrafish, disruption of inhibitory neurons via En1 loss of function affects the range of tail movement, not just its frequency, supporting species-specific V1 regulation of the tail.

For the limb as well, species-specific differences exist between vertebrates. Frogs, in contrast to mice, are not weight bearing,[22] lack classic mammalian gaits[102,103] and fine-motor skills,[104] and move via bilateral synchronous kicking.[102,105] One attractive source of this divergence in coordination that emerges from our study is fine-scale differences in the number, position, and molecular identity of interneuron subtypes. In mice, such differences can relate to variant descending, sensory, and motor inputs,[9,12,106] and consistent with this, frogs reportedly lack a corticospinal tract[107] and gamma MNs.[108,109] This observation, in combination with recent advances in neural circuit visualization and manipulation,[83,110,111] prioritizes similar evaluation of interneuron subtypes, anatomy, and function in other understudied vertebrates.

Taken together, our study of motor circuits during frog metamorphosis demonstrates that the emergence of limb-based movement is accompanied by an increase in inhibitory neuron number and diversity of cell types. We reveal highly conserved cellular building blocks that span distant limbed vertebrates but exhibit species-specific adaptations by motor behavior type. This mechanistic insight into how spinal circuits adapt to swim versus limb movement in one species' development provides a framework for understanding analogous adaptations across species during aquatic-to-terrestrial evolution of the vertebrate spinal cord.

Limitations of the study

Aligning developmental stages between two species from different vertebrate classes, especially those developing in distinct environments (*in utero* for mice versus *ex utero* for frogs) presents a challenge. For our cross-species comparison of cell types, we focused on the stages characterized by the peak of motor and interneuron generation: *Xenopus* NF54–58 (see the time course in Figure S4) and mouse embryonic stages E13.5–P0.[9,51,56,70] These stages are also comparable in terms of limb development and muscle innervation.[112]

Due to the long generation time of *Xenopus* (>1 year to sexual maturity), our loss-of-function analysis was conducted using first-generation (F0) CRISPR-edited animals and compared to uninjected controls. In frogs, F0 CRISPR generates consistently high mutation rates,[83,113] as validated by genotyping and immunohistochemistry and described in the STAR Methods. FoxP1 and En1 CRISPR mutants were concurrently generated, scored for the same movement features, and exhibited distinct, non-overlapping phenotypes, arguing against non-specific or off-target effects of the CRISPR-Cas9 machinery.

Finally, our study establishes a link between frog behavior and cellular changes in the spinal circuitry. The observed loss of one V1 subtype and not other V1 clades or cardinal interneuron types supports subtype-specific regulation of frequency. We do not rule out, however, the contribution of other circuit-level changes, such as those in connectivity, which currently lie beyond the scope of existing methodologies. In addition, while we characterized a diverse array of motor behavior patterns during frog development (e.g., escape swimming, free swimming, turning, straight-line and free movement in a circular arena, etc.), we recognize that the frog locomotor repertoire comprises other movements not described here (e.g., scratching, scooping, and asynchronous escape on land). Further analysis of such stimulus- or context-dependent behaviors may reveal additional functions of limb-associated cell types.

RESOURCE AVAILABILITY

Lead contact

Further information and requests for resources and reagents should be directed to and will be fulfilled by the lead contact, Lora B. Sweeney (lora.sweeney@ist.ac.at).

Materials availability

This study generated several *Xenopus* antibodies and transgenic lines. The materials will be made available upon request by the lead contact, Lora B. Sweeney (lora.sweeney@ist.ac.at).

Data and code availability

- The single-cell RNA sequencing datasets generated in this study have been deposited in the Gene Expression Omnibus (GEO) and are publicly available under accession number GSE294631 (https://www.ncbi.nlm.nih.gov/geo/query/acc.cgi?acc=GSE294631).
- Code used for behavioral analysis is available at GitHub (https://github.com/sweeneylab/MN_V1_analysis) and archived at Zenodo (https://doi.org/10.5281/zenodo.18755393). Code used for single-cell analysis is available at GitHub (https://github.com/yuriignatyev/V1sMNs_metamorphosis) and archived at Zenodo (https://doi.org/10.5281/zenodo.18683732). The HCR quantification pipeline is available at Institute of Science and Technology Austria (ISTA) GitLab (https://git.ista.ac.at/iof-group/image-analysis/HCR-SpeckleQuantification) and archived at Zenodo (https://doi.org/10.5281/zenodo.18759665).
- Any additional information required to reanalyze the data reported in this paper is available from the lead contact upon request.

ACKNOWLEDGMENTS

We would like to thank the members of the Sweeney Lab, Mario de Bono, Michael Forsthofer, Katharina Lust, and Meital Oren, for comments on the manuscript. We are also grateful to Tom Jessell and Chris Kintner for their scientific insight and mentorship during the conception of this project. It would also have not been possible without the technical support of the Aquatics and Imaging and Optics Facility support teams (ISTA). We thank Martin Estermann for preparing the initial draft of the graphical abstract and Niki Barolini for the final version. In addition, we thank our funding sources for providing the resources to do these experiments: GFF NÖ FTI Strategy Lower Austria dissertation grant FT121-D-046 (to D.V.), Horizon Europe ERC starting grant 101041551 (to Y.I., L.B.S., F.A.T., and D.V.), Special Research Program (SFB) of the Austrian Science Fund (FWF) project F7814-B (to L.B.S.), Austrian Science Fund (FWF) 10.55776/COE16 (to Y.I. and L.B.S.), NINDS 5R35NS116858 (to J.S.D.), CZI grant DAF2020-225401 (DOI) 10.37921/120055ratwvi (to R.H.), NIH grant R01NS123116 (to J.B.B.), American Lebanese Syrian Associated Charities (ALSAC) (to J.B.B.), German Academic Exchange Service (DAAD) IFI grant 57515251-91853472 (to Z.H.), and Project A.L.S. (to S.B.-M.).

AUTHOR CONTRIBUTIONS

L.B.S. led and coordinated the project. D.V., F.A.T., Y.I., Z.P.M.H., A.J.T., P.C., M.J.J., M.I.G., and L.B.S. implemented experiments. D.V., Y.I., M.I.G., and L.B.S. led *Xenopus* cell type data collection and analysis. F.A.T., Z.H., and M.J.J. collected all behavioral data in close collaboration with R.H. and C.S., who designed the behavioral imaging setup and analysis pipeline, respectively. D.V. and F.A.T. collected all HCR data, and M.S. and M.D.V. designed and implemented the analysis pipeline. A.T., P.C., and J.B.B. collected all mouse data. S.B.-M. generated antibodies. D.V., F.A.T., Y.I., C.S., and L.B.S. wrote the manuscript. J.D., J.B.B., S.B-M., and M.I.G. edited the manuscript and provided critical feedback on the project.

DECLARATION OF INTERESTS

The authors declare no competing interests.

DECLARATION OF GENERATIVE AI AND AI-ASSISTED TECHNOLOGIES IN THE WRITING PROCESS

During the preparation of this work, the authors used ChatGPT to brainstorm alternative, more concise language. After using this tool or service, the authors reviewed and edited the content as needed and take full responsibility for the content of the publication.

STAR★METHODS

Detailed methods are provided in the online version of this paper and include the following:

- KEY RESOURCES TABLE
- EXPERIMENTAL MODEL AND STUDY PARTICIPANT DETAILS
- METHOD DETAILS
  - Single cell RNA sequencing (scRNAseq)
  - Antibodies
  - Immunohistochemistry and microscopy of frog tissue
  - Immunohistochemistry and microscopy of mouse tissue
  - Retrograde labeling
  - *Xenopus* transgenesis
  - CRISPR-Cas9 knockout generation
  - sgRNA design
  - *Xenopus laevis* genotyping
  - Behavioral setup and video recording
  - Pose estimation by SLEAP
  - Quantification of behavior
  - Frequency analysis
  - Animal pose visualization using PCA
  - Extraction of straight-line movement episodes
- QUANTIFICATION AND STATISTICAL ANALYSIS
  - Behavioral tracking statistics
  - Cell-type quantification
  - Spatial plotting
  - Entropy analysis
  - Cell-type statistics
  - HCR quantification
  - HCR quantification statistics

SUPPLEMENTAL INFORMATION

Supplemental information can be found online at https://doi.org/10.1016/j.celrep.2026.117227.

Received: May 7, 2025
Revised: January 16, 2026
Accepted: March 16, 2026
Published: April 10, 2026

REFERENCES

1. Grillner, S., and El Manira, A. (2020). Current Principles of Motor Control, with Special Reference to Vertebrate Locomotion. Physiol. Rev. *100*, 271–320. https://doi.org/10.1152/physrev.00015.2019.
2. (2018). Physical and Biological Properties and Principles: Related to Animal Locomotion. In Animal Locomotion, A. Biewener, S. Patek, A.A. Biewener, and S.N. Patek, eds. (Oxford University Press), p. 0. https://doi.org/10.1093/oso/9780198743156.003.0001.
3. Gordon, M.S., Blickhan, R., Dabiri, J.O., and Videler, J.J. (2017). In Animal Locomotion: Physical Principles and Adaptations, First Edition (CRC Press). https://doi.org/10.1201/b22011.
4. Gosgnach, S., Bikoff, J.B., Dougherty, K.J., El Manira, A., Lanuza, G.M., and Zhang, Y. (2017). Delineating the Diversity of Spinal Interneurons in Locomotor Circuits. J. Neurosci. *37*, 10835–10841. https://doi.org/10.1523/JNEUROSCI.1829-17.2017.
5. Dasen, J.S. (2022). Establishing the Molecular and Functional Diversity of Spinal Motoneurons. In Vertebrate Motoneurons Advances in Neurobiology, M.J. O'Donovan and M. Falgairolle, eds. (Springer International Publishing), pp. 3–44. https://doi.org/10.1007/978-3-031-07167-6_1.
6. Wilson, A.C., and Sweeney, L.B. (2023). Spinal cords: Symphonies of interneurons across species. Front. Neural Circuits *17*, 1146449. https://doi.org/10.3389/fncir.2023.1146449.
7. Bagnall, M.W., and McLean, D.L. (2014). Modular organization of axial microcircuits in zebrafish. Science *343*, 197–200. https://doi.org/10.1126/science.1245629.
8. El Manira, A. (2023). Modular circuit organization for speed control of locomotor movements. Curr. Opin. Neurobiol. *82*, 102760. https://doi.org/10.1016/j.conb.2023.102760.
9. Bikoff, J.B., Gabitto, M.I., Rivard, A.F., Drobac, E., Machado, T.A., Miri, A., Brenner-Morton, S., Famojure, E., Diaz, C., Alvarez, F.J., et al. (2016). Spinal Inhibitory Interneuron Diversity Delineates Variant Motor Microcircuits. Cell *165*, 207–219. https://doi.org/10.1016/j.cell.2016.01.027.
10. Gabitto, M.I., Pakman, A., Bikoff, J.B., Abbott, L.F., Jessell, T.M., and Paninski, L. (2016). Bayesian Sparse Regression Analysis Documents the Diversity of Spinal Inhibitory Interneurons. Cell *165*, 220–233. https://doi.org/10.1016/j.cell.2016.01.026.
11. Sweeney, L.B., Bikoff, J.B., Gabitto, M.I., Brenner-Morton, S., Baek, M., Yang, J.H., Tabak, E.G., Dasen, J.S., Kintner, C.R., and Jessell, T.M. (2018). Origin and Segmental Diversity of Spinal Inhibitory Interneurons. Neuron *97*, 341–355.e3. https://doi.org/10.1016/j.neuron.2017.12.029.
12. Worthy, A.E., Anderson, J.T., Lane, A.R., Gomez-Perez, L.J., Wang, A.A., Griffith, R.W., Rivard, A.F., Bikoff, J.B., and Alvarez, F.J. (2024). Spinal V1 inhibitory interneuron clades differ in birthdate, projections to motoneurons, and heterogeneity. eLife *13*, RP95172. https://doi.org/10.7554/eLife.95172.
13. Hayashi, M., Hinckley, C.A., Driscoll, S.P., Moore, N.J., Levine, A.J., Hilde, K.L., Sharma, K., and Pfaff, S.L. (2018). Graded Arrays of Spinal and Supraspinal V2a Interneuron Subtypes Underlie Forelimb and Hindlimb Motor Control. Neuron *97*, 869–884.e5.
14. Hayashi, M., Gullo, M., Senturk, G., Di Costanzo, S., Nagasaki, S.C., Kageyama, R., Imayoshi, I., Goulding, M., Pfaff, S.L., and Gatto, G. (2023). A spinal synergy of excitatory and inhibitory neurons coordinates ipsilateral body movements. eLife *12*. https://doi.org/10.7554/eLife.89362.1.
15. Borowska, J., Jones, C.T., Zhang, H., Blacklaws, J., Goulding, M., and Zhang, Y. (2013). Functional Subpopulations of V3 Interneurons in the Mature Mouse Spinal Cord. J. Neurosci. *33*, 18553–18565. https://doi.org/10.1523/JNEUROSCI.2005-13.2013.
16. Deska-Gauthier, D., Borowska-Fielding, J., Jones, C., Zhang, H., MacKay, C.S., Michail, R., Bennett, L.A., Bikoff, J.B., and Zhang, Y. (2024). Embryonic temporal-spatial delineation of excitatory spinal V3 interneuron diversity. Cell Rep. *43*, 113635. https://doi.org/10.1016/j.celrep.2023.113635.
17. Osseward, P.J., Amin, N.D., Moore, J.D., Temple, B.A., Barriga, B.K., Bachmann, L.C., Beltran, F., Gullo, M., Clark, R.C., Driscoll, S.P., et al. (2021). Conserved genetic signatures parcellate cardinal spinal neuron classes into local and projection subsets. Science *372*, 385–393. https://doi.org/10.1126/science.abe0690.
18. Sengupta, M., and Bagnall, M.W. (2023). Spinal Interneurons: Diversity and Connectivity in Motor Control. Annu. Rev. Neurosci. *46*, 79–99. https://doi.org/10.1146/annurev-neuro-083122-025325.
19. Zhang, J., Lanuza, G.M., Britz, O., Wang, Z., Siembab, V.C., Zhang, Y., Velasquez, T., Alvarez, F.J., Frank, E., and Goulding, M. (2014). V1 and v2b interneurons secure the alternating flexor-extensor motor activity mice require for limbed locomotion. Neuron *82*, 138–150. https://doi.org/10.1016/j.neuron.2014.02.013.
20. Trevisan, A.J., Han, K., Chapman, P., Kulkarni, A.S., Hinton, J.M., Ramirez, C., Klein, I., Gatto, G., Gabitto, M.I., Menon, V., and Bikoff, J.B. (2024). The transcriptomic landscape of spinal V1 interneurons reveals a role for En1 in specific elements of motor output. Preprint at bioRxiv. https://doi.org/10.1101/2024.09.18.613279.
21. Gray, L.A., O'Reilly, J.C., and Nishikawa, K.C. (1997). Evolution of forelimb movement patterns for prey manipulation in anurans. J. Exp. Zool. *277*, 417–424. https://doi.org/10.1002/(sici)1097-010x(19970415)277:6%253C417::aid-jez1%253E3.0.co;2-r.

22. Li, M., Gao, Z., Wang, J., Song, W., Zhang, Q., Tong, J., and Ren, L. (2021). Cooperation behavior of fore- And hindlimbs during jumping in Rana dybowskii and Xenopus laevis. Ecol. Evol. *11*, 7569–7578. https://doi.org/10.1002/ece3.7589.
23. Sillar, K.T., Simmers, J., and Combes, D. (2023). From tadpole to adult frog locomotion. Curr. Opin. Neurobiol. *82*, 102753. https://doi.org/10.1016/j.conb.2023.102753.
24. Pereira, T.D., Aldarondo, D.E., Willmore, L., Kislin, M., Wang, S.S.-H., Murthy, M., and Shaevitz, J.W. (2019). Fast animal pose estimation using deep neural networks. Nat. Methods *16*, 117–125. https://doi.org/10.1038/s41592-018-0234-5.
25. Pereira, T.D., Tabris, N., Matsliah, A., Turner, D.M., Li, J., Ravindranath, S., Papadoyannis, E.S., Normand, E., Deutsch, D.S., Wang, Z.Y., et al. (2022). SLEAP: A deep learning system for multi-animal pose tracking. Nat. Methods *19*, 486–495. https://doi.org/10.1038/s41592-022-01426-1.
26. Nieuwkoop, P.D., and Faber, J. (1994). Normal Table of Xenopus Laevis (Daudin): A Systematical and Chronological Survey of the Development from the Fertilized Egg till the End of Metamorphosis. Garland Pub. https://doi.org/10.1201/9781003064565.
27. Hughes, A., and Prestige, M.C. (1967). Development of behaviour in the hindlimb of Xenopus laevis. J. Zool. *152*, 347–359. https://doi.org/10.1111/j.1469-7998.1967.tb01649.x.
28. Marsh-Armstrong, N., Cai, L., and Brown, D.D. (2004). Thyroid hormone controls the development of connections between the spinal cord and limbs during Xenopus laevis metamorphosis. Proc. Natl. Acad. Sci. USA *101*, 165–170. https://doi.org/10.1073/pnas.2136755100.
29. Zahn, N., James-Zorn, C., Ponferrada, V.G., Adams, D.S., Grzymkowski, J., Buchholz, D.R., Nascone-Yoder, N.M., Horb, M., Moody, S.A., Vize, P.D., and Zorn, A.M. (2022). Normal Table of Xenopus development: a new graphical resource. Development *149*, dev200356. https://doi.org/10.1242/dev.200356.
30. Boothby, K.M., and Roberts, A. (1995). Effects of site of tactile stimulation on the escape swimming responses of hatchling Xenopus laevis embryos. J. Zool. *235*, 113–125. https://doi.org/10.1111/j.1469-7998.1995.tb05132.x.
31. Scharf, I., and Farji-Brener, A. (2024). Wall-following behavior: Its ultimate and proximate explanations, prevalence, and implications. In Advances in the Study of Behavior, J. Podos and S. Healy, eds. (Elsevier), pp. 1–49. https://doi.org/10.1016/bs.asb.2024.02.003.
32. Wells, K.D. (2007). The Ecology and Behavior of Amphibians (University of Chicago Press). https://doi.org/10.7208/chicago/9780226893334.001.0001.
33. Bellardita, C., and Kiehn, O. (2015). Phenotypic characterization of speed-associated gait changes in mice reveals modular organization of locomotor networks. Curr. Biol. *25*, 1426–1436. https://doi.org/10.1016/j.cub.2015.04.005.
34. Combes, D., Merrywest, S.D., Simmers, J., and Sillar, K.T. (2004). Developmental segregation of spinal networks driving axial- and hindlimb-based locomotion in metamorphosing Xenopus laevis. J. Physiol. *559*, 17–24. https://doi.org/10.1113/jphysiol.2004.069542.
35. Roberts, A., Li, W.-C., and Soffe, S.R. (2008). Roles for inhibition: studies on networks controlling swimming in young frog tadpoles. J. Comp. Physiol. A Neuroethol. Sens. Neural Behav. Physiol. *194*, 185–193. https://doi.org/10.1007/s00359-007-0273-3.
36. Currie, S.P., Combes, D., Scott, N.W., Simmers, J., and Sillar, K.T. (2016). A behaviorally related developmental switch in nitrergic modulation of locomotor rhythmogenesis in larval Xenopus tadpoles. J. Neurophysiol. *115*, 1446–1457. https://doi.org/10.1152/jn.00283.2015.
37. Lambert, F.M., Cardoit, L., Courty, E., Bougerol, M., Thoby-Brisson, M., Simmers, J., Tostivint, H., and Le Ray, D. (2018). Functional limb muscle innervation prior to cholinergic transmitter specification during early metamorphosis in Xenopus. eLife *7*, e30693. https://doi.org/10.7554/eLife.30693.
38. Combes, D., Sillar, K.T., and Simmers, J. (2020). Xenopus frog metamorphosis: A model for studying locomotor network development and neuromodulation. In The Neural Control of Movement, P.J. Whelan and S.A. Sharples, eds. (Academic Press), pp. 175–203. https://doi.org/10.1016/B978-0-12-816477-8.00008-9.
39. Currie, S.P., and Sillar, K.T. (2018). Developmental changes in spinal neuronal properties, motor network configuration, and neuromodulation at free-swimming stages of Xenopus tadpoles. J. Neurophysiol. *119*, 786–795. https://doi.org/10.1152/jn.00219.2017.
40. Richter, K., Grunz, H., and Dawid, I.B. (1988). Gene expression in the embryonic nervous system of Xenopus laevis. Proc. Natl. Acad. Sci. USA *85*, 8086–8090. https://doi.org/10.1073/pnas.85.21.8086.
41. Oschwald, R., Richter, K., and Grunz, H. (1991). Localization of a nervous system-specific class II beta-tubulin gene in Xenopus laevis embryos by whole-mount in situ hybridization. Int. J. Dev. Biol. *35*, 399–405.
42. Huang, J.K., Dorey, K., Ishibashi, S., and Amaya, E. (2007). BDNF promotes target innervation of Xenopus mandibular trigeminal axons in vivo. BMC Dev. Biol. *7*, 59. https://doi.org/10.1186/1471-213X-7-59.
43. Bikoff, J.B. (2019). Interneuron diversity and function in the spinal motor system. Curr. Opin. Physiol. *8*, 36–43. https://doi.org/10.1016/j.cophys.2018.12.013.
44. Burrill, J.D., Moran, L., Goulding, M.D., and Saueressig, H. (1997). PAX2 is expressed in multiple spinal cord interneurons, including a population of EN1+ interneurons that require PAX6 for their development. Development *124*, 4493–4503. https://doi.org/10.1242/dev.124.22.4493.
45. Higashijima, S.i., Masino, M.A., Mandel, G., and Fetcho, J.R. (2004). Engrailed-1 expression marks a primitive class of inhibitory spinal interneuron. J. Neurosci. *24*, 5827–5839. https://doi.org/10.1523/JNEUROSCI.5342-03.2004.
46. Ericson, J., Thor, S., Edlund, T., Jessell, T.M., and Yamada, T. (1992). Early stages of motor neuron differentiation revealed by expression of homeobox gene Islet-1. Science *256*, 1555–1560. https://doi.org/10.1126/science.1350865.
47. Pfaff, S.L., Mendelsohn, M., Stewart, C.L., Edlund, T., and Jessell, T.M. (1996). Requirement for LIM homeobox gene Isl1 in motor neuron generation reveals a motor neuron-dependent step in interneuron differentiation. Cell *84*, 309–320. https://doi.org/10.1016/s0092-8674(00)80985-x.
48. Arber, S., Han, B., Mendelsohn, M., Smith, M., Jessell, T.M., and Sockanathan, S. (1999). Requirement for the homeobox gene Hb9 in the consolidation of motor neuron identity. Neuron *23*, 659–674. https://doi.org/10.1016/s0896-6273(01)80026-x.
49. Thaler, J., Harrison, K., Sharma, K., Lettieri, K., Kehrl, J., and Pfaff, S.L. (1999). Active suppression of interneuron programs within developing motor neurons revealed by analysis of homeodomain factor HB9. Neuron *23*, 675–687. https://doi.org/10.1016/s0896-6273(01)80027-1.
50. Roberts, A., Walford, A., Soffe, S.r., and Yoshida, M. (1999). Motoneurons of the axial swimming muscles in hatchling Xenopus tadpoles: Features, distribution, and central synapses. J. Comp. Neurol. *411*, 472–486. https://doi.org/10.1002/(SICI)1096-9861(19990830)411:3%-253C472::AID-CNE9%253E3.0.CO;2-B.
51. Agalliu, D., Takada, S., Agalliu, I., McMahon, A.P., and Jessell, T.M. (2009). Motor neurons with axial muscle projections specified by Wnt4/5 signaling. Neuron *61*, 708–720. https://doi.org/10.1016/j.neuron.2008.12.026.
52. Tsuchida, T., Ensini, M., Morton, S.B., Baldassare, M., Edlund, T., Jessell, T.M., and Pfaff, S.L. (1994). Topographic organization of embryonic motor neurons defined by expression of LIM homeobox genes. Cell *79*, 957–970. https://doi.org/10.1016/0092-8674(94)90027-2.
53. Sharma, K., Sheng, H.Z., Lettieri, K., Li, H., Karavanov, A., Potter, S., Westphal, H., and Pfaff, S.L. (1998). LIM Homeodomain Factors Lhx3 and Lhx4 Assign Subtype Identities for Motor Neurons. Cell *95*, 817–828. https://doi.org/10.1016/S0092-8674(00)81704-3.

54. Sharma, K., Leonard, A.E., Lettieri, K., and Pfaff, S.L. (2000). Genetic and epigenetic mechanisms contribute to motor neuron pathfinding. Nature *406*, 515–519. https://doi.org/10.1038/35020078.

55. Nishikawa, A., and Hayashi, H. (1994). Isoform transition of contractile proteins related to muscle remodeling with an axial gradient during metamorphosis in Xenopus laevis. Dev. Biol. *165*, 86–94. https://doi.org/10.1006/dbio.1994.1236.

56. Dasen, J.S., De Camilli, A., Wang, B., Tucker, P.W., and Jessell, T.M. (2008). Hox Repertoires for Motor Neuron Diversity and Connectivity Gated by a Single Accessory Factor, FoxP1. Cell *134*, 304–316. https://doi.org/10.1016/j.cell.2008.06.019.

57. Blitz, I.L., Andelfinger, G., and Horb, M.E. (2006). Germ layers to organs: Using Xenopus to study "later" development. Semin. Cell Dev. Biol. *17*, 133–145. https://doi.org/10.1016/j.semcdb.2005.11.002.

58. D'Elia, K.P., and Dasen, J.S. (2018). Development, functional organization, and evolution of vertebrate axial motor circuits. Neural Dev. *13*, 10. https://doi.org/10.1186/s13064-018-0108-7.

59. Tanabe, Y., William, C., and Jessell, T.M. (1998). Specification of Motor Neuron Identity by the MNR2 Homeodomain Protein. Cell *95*, 67–80. https://doi.org/10.1016/S0092-8674(00)81783-3.

60. Sockanathan, S., and Jessell, T.M. (1998). Motor neuron-derived retinoid signaling specifies the subtype identity of spinal motor neurons. Cell *94*, 503–514. https://doi.org/10.1016/s0092-8674(00)81591-3.

61. Mendelsohn, A.I., Dasen, J.S., and Jessell, T.M. (2017). Divergent Hox Coding and Evasion of Retinoid Signaling Specifies Motor Neurons Innervating Digit Muscles. Neuron *93*, 792–805.e4. https://doi.org/10.1016/j.neuron.2017.01.017.

62. Dasen, J.S., Tice, B.C., Brenner-Morton, S., and Jessell, T.M. (2005). A Hox regulatory network establishes motor neuron pool identity and target-muscle connectivity. Cell *123*, 477–491. https://doi.org/10.1016/j.cell.2005.09.009.

63. Amin, N.D., Bai, G., Klug, J.R., Bonanomi, D., Pankratz, M.T., Gifford, W.D., Hinckley, C.A., Sternfeld, M.J., Driscoll, S.P., Dominguez, B., et al. (2015). Loss of motoneuron-specific microRNA-218 causes systemic neuromuscular failure. Science *350*, 1525–1529. https://doi.org/10.1126/science.aad2509.

64. Falgairolle, M., and O'Donovan, M.J. (2019). V1 interneurons regulate the pattern and frequency of locomotor-like activity in the neonatal mouse spinal cord. PLoS Biol. *17*, e3000447. https://doi.org/10.1371/journal.pbio.3000447.

65. Gosgnach, S., Lanuza, G.M., Butt, S.J.B., Saueressig, H., Zhang, Y., Velasquez, T., Riethmacher, D., Callaway, E.M., Kiehn, O., and Goulding, M. (2006). V1 spinal neurons regulate the speed of vertebrate locomotor outputs. Nature *440*, 215–219. https://doi.org/10.1038/nature04545.

66. Kimura, Y., and Higashijima, S.I. (2019). Regulation of locomotor speed and selection of active sets of neurons by V1 neurons. Nat. Commun. *10*, 2268. https://doi.org/10.1038/s41467-019-09871-x.

67. Benito-Gonzalez, A., and Alvarez, F.J. (2012). Renshaw cells and Ia inhibitory interneurons are generated at different times from p1 progenitors and differentiate shortly after exiting the cell cycle. J. Neurosci. *32*, 1156–1170. https://doi.org/10.1523/JNEUROSCI.3630-12.2012.

68. Britz, O., Zhang, J., Grossmann, K.S., Dyck, J., Kim, J.C., Dymecki, S., Gosgnach, S., and Goulding, M. (2015). A genetically defined asymmetry underlies the inhibitory control of flexor-extensor locomotor movements. eLife *4*, e04718. https://doi.org/10.7554/eLife.04718.

69. Saueressig, H., Burrill, J., and Goulding, M. (1999). Engrailed-1 and Netrin-1 regulate axon pathfinding by association interneurons that project to motor neurons. Development *126*, 4201–4212. https://doi.org/10.1242/dev.126.19.4201.

70. Delile, J., Rayon, T., Melchionda, M., Edwards, A., Briscoe, J., and Sagner, A. (2019). Single cell transcriptomics reveals spatial and temporal dynamics of gene expression in the developing mouse spinal cord. Development *146*, dev173807. https://doi.org/10.1242/dev.173807.

71. Francius, C., Harris, A., Rucchin, V., Hendricks, T.J., Stam, F.J., Barber, M., Kurek, D., Grosveld, F.G., Pierani, A., Goulding, M., and Clotman, F. (2013). Identification of multiple subsets of ventral interneurons and differential distribution along the rostrocaudal axis of the developing spinal cord. PLoS One *8*, e70325. https://doi.org/10.1371/journal.pone.0070325.

72. Rayon, T., Maizels, R.J., Barrington, C., and Briscoe, J. (2021). Single-cell transcriptome profiling of the human developing spinal cord reveals a conserved genetic programme with human-specific features. Development *148*, dev199711. https://doi.org/10.1242/dev.199711.

73. Russ, D.E., Cross, R.B.P., Li, L., Koch, S.C., Matson, K.J.E., Yadav, A., Alkaslasi, M.R., Lee, D.I., Le Pichon, C.E., Menon, V., and Levine, A.J. (2021). A harmonized atlas of mouse spinal cord cell types and their spatial organization. Nat. Commun. *12*, 5722. https://doi.org/10.1038/s41467-021-25125-1.

74. Alvarez, F.J., and Fyffe, R.E.W. (2007). The continuing case for the Renshaw cell. J. Physiol. *584*, 31–45. https://doi.org/10.1113/jphysiol.2007.136200.

75. Stam, F.J., Hendricks, T.J., Zhang, J., Geiman, E.J., Francius, C., Labosky, P.A., Clotman, F., and Goulding, M. (2012). Renshaw cell interneuron specialization is controlled by a temporally restricted transcription factor program. Development *139*, 179–190. https://doi.org/10.1242/dev.071134.

76. Li, W.-C., Higashijima, S.i., Parry, D.M., Roberts, A., and Soffe, S.R. (2004). Primitive Roles for Inhibitory Interneurons in Developing Frog Spinal Cord. J. Neurosci. *24*, 5840–5848. https://doi.org/10.1523/JNEUROSCI.1633-04.2004.

77. Martin, B.L., and Harland, R.M. (2001). Hypaxial muscle migration during primary myogenesis in Xenopus laevis. Dev. Biol. *239*, 270–280. https://doi.org/10.1006/dbio.2001.0434.

78. van Mier, P., and ten Donkelaar, H.J. (1988). The development of primary afferents to the lumbar spinal cord in Xenopus laevis. Neurosci. Lett. *84*, 35–40. https://doi.org/10.1016/0304-3940(88)90333-3.

79. Martínez, O., and Reyes-Valdés, M.H. (2008). Defining diversity, specialization, and gene specificity in transcriptomes through information theory. Proc. Natl. Acad. Sci. USA *105*, 9709–9714. https://doi.org/10.1073/pnas.0803479105.

80. Dasen, J.S., and Jessell, T.M. (2009). Hox networks and the origins of motor neuron diversity. Curr. Top. Dev. Biol. *88*, 169–200. https://doi.org/10.1016/S0070-2153(09)88006-X.

81. Rousso, D.L., Gaber, Z.B., Wellik, D., Morrisey, E.E., and Novitch, B.G. (2008). Coordinated actions of the forkhead protein Foxp1 and Hox proteins in the columnar organization of spinal motor neurons. Neuron *59*, 226–240. https://doi.org/10.1016/j.neuron.2008.06.025.

82. Sürmeli, G., Akay, T., Ippolito, G.C., Tucker, P.W., and Jessell, T.M. (2011). Patterns of spinal sensory-motor connectivity prescribed by a dorsoventral positional template. Cell *147*, 653–665. https://doi.org/10.1016/j.cell.2011.10.012.

83. Willsey, H.R., Exner, C.R.T., Xu, Y., Everitt, A., Sun, N., Wang, B., Dea, J., Schmunk, G., Zaltsman, Y., Teerikorpi, N., et al. (2021). Parallel in vivo analysis of large-effect autism genes implicates cortical neurogenesis and estrogen in risk and resilience. Neuron *109*, 788–804.e8. https://doi.org/10.1016/j.neuron.2021.01.002.

84. Alvarez, F.J., Jonas, P.C., Sapir, T., Hartley, R., Berrocal, M.C., Geiman, E.J., Todd, A.J., and Goulding, M. (2005). Postnatal phenotype and localization of spinal cord V1 derived interneurons. J. Comp. Neurol. *493*, 177–192. https://doi.org/10.1002/cne.20711.

85. Yao, M., Nagamori, A., CamposMaçãsS., Azim, E., Sharpee, T., Goulding, M., Golomb, D., and Gatto, G. (2025). The spinal premotor network driving scratching flexor and extensor alternation. Cell Reports *44*, 115845. https://doi.org/10.1016/j.celrep.2025.115845.

86. Peyrot, S.M., Martin, B.L., and Harland, R.M. (2010). Lymph heart musculature is under distinct developmental control from lymphatic

endothelium. Dev. Biol. *339*, 429–438. https://doi.org/10.1016/j.ydbio.2010.01.002.

87. Andersson, L.S., Larhammar, M., Memic, F., Wootz, H., Schwochow, D., Rubin, C.-J., Patra, K., Arnason, T., Wellbring, L., Hjälm, G., et al. (2012). Mutations in DMRT3 affect locomotion in horses and spinal circuit function in mice. Nature *488*, 642–646. https://doi.org/10.1038/nature11399.
88. Ericson, J., Rashbass, P., Schedl, A., Brenner-Morton, S., Kawakami, A., Van Heyningen, V., Jessell, T.M., and Briscoe, J. (1997). Pax6 Controls Progenitor Cell Identity and Neuronal Fate in Response to Graded Shh Signaling. Cell *90*, 169–180. https://doi.org/10.1016/S0092-8674(00)80323-2.
89. Hobert, O., and Kratsios, P. (2019). Neuronal identity control by terminal selectors in worms, flies, and chordates. Curr. Opin. Neurobiol. *56*, 97–105. https://doi.org/10.1016/j.conb.2018.12.006.
90. Dasen, J.S., Liu, J.-P., and Jessell, T.M. (2003). Motor neuron columnar fate imposed by sequential phases of Hox-c activity. Nature *425*, 926–933.
91. Furlow, J.D., and Neff, E.S. (2006). A developmental switch induced by thyroid hormone: Xenopus laevis metamorphosis. Trends Endocrinol. Metab. *17*, 40–47. https://doi.org/10.1016/j.tem.2006.01.007.
92. Schlosser, G., Koyano-Nakagawa, N., and Kintner, C. (2002). Thyroid hormone promotes neurogenesis in the Xenopus spinal cord. Dev. Dyn. *225*, 485–498. https://doi.org/10.1002/dvdy.10179.
93. Bernal, J. (2007). Thyroid hormone receptors in brain development and function. Nat. Clin. Pract. Endocrinol. Metab. *3*, 249–259. https://doi.org/10.1038/ncpendmet0424.
94. Rapti, G., Li, C., Shan, A., Lu, Y., and Shaham, S. (2017). Glia initiate brain assembly through noncanonical Chimaerin–Furin axon guidance in C. elegans. Nat. Neurosci. *20*, 1350–1360. https://doi.org/10.1038/nn.4630.
95. Sweeney, L.B., Couto, A., Chou, Y.-H., Berdnik, D., Dickson, B.J., Luo, L., and Komiyama, T. (2007). Temporal target restriction of olfactory receptor neurons by Semaphorin-1a/PlexinA-mediated axon-axon interactions. Neuron *53*, 185–200. https://doi.org/10.1016/j.neuron.2006.12.022.
96. Keshishian, H. (1980). The origin and morphogenesis of pioneer neurons in the grasshopper metathoracic leg. Dev. Biol. *80*, 388–397. https://doi.org/10.1016/0012-1606(80)90413-3.
97. Schoch, R.R. (2014). Amphibian Evolution: The Life of Early Land Vertebrates, 1st ed. (Wiley). https://doi.org/10.1002/9781118759127.
98. Wallén, P., Grillner, S., Feldman, J.L., and Bergelt, S. (1985). Dorsal and ventral myotome motoneurons and their input during fictive locomotion in lamprey. J. Neurosci. *5*, 654–661. https://doi.org/10.1523/JNEUROSCI.05-03-00654.1985.
99. Fetcho, J.R. (1987). A review of the organization and evolution of motoneurons innervating the axial musculature of vertebrates. Brain Res. *434*, 243–280. https://doi.org/10.1016/0165-0173(87)90001-4.
100. Roberts, A., Li, W.-C., and Soffe, S.R. (2010). How neurons generate behavior in a hatchling amphibian tadpole: an outline. Front. Behav. Neurosci. *4*, 16. https://doi.org/10.3389/fnbeh.2010.00016.
101. Jung, H., Baek, M., D'Elia, K.P., Boisvert, C., Currie, P.D., Tay, B.-H., Venkatesh, B., Brown, S.M., Heguy, A., Schoppik, D., and Dasen, J.S. (2018). The Ancient Origins of Neural Substrates for Land Walking. Cell *172*, 667–682.e15. https://doi.org/10.1016/j.cell.2018.01.013.
102. Nauwelaerts, S., and Aerts, P. (2002). Two distinct gait types in swimming frogs. J. Zool. *258*, 183–188. https://doi.org/10.1017/S0952836902001292.
103. Stehouwer, D.J., and Farel, P.B. (1985). Development of locomotor mechanisms in the frog. J. Neurophysiol. *53*, 1453–1466. https://doi.org/10.1152/jn.1985.53.6.1453.
104. Giszter, S.F., McIntyre, J., and Bizzi, E. (1989). Kinematic strategies and sensorimotor transformations in the wiping movements of frogs. J. Neurophysiol. *62*, 750–767. https://doi.org/10.1152/jn.1989.62.3.750.
105. Rauscent, A., Le Ray, D., Cabirol-Pol, M.-J., Sillar, K.T., Simmers, J., and Combes, D. (2006). Development and neuromodulation of spinal locomotor networks in the metamorphosing frog. J. Physiol. Paris *100*, 317–327. https://doi.org/10.1016/j.jphysparis.2007.05.009.
106. Chapman, P.D., Kulkarni, A.S., Trevisan, A.J., Han, K., Hinton, J.M., Deltuvaite, P., Fenno, L.E., Ramakrishnan, C., Patton, M.H., Schwarz, L.A., et al. (2025). A brain-wide map of descending inputs onto spinal V1 interneurons. Neuron *113*, 524–538.e6. https://doi.org/10.1016/j.neuron.2024.11.019.
107. Iwaniuk, A.N., and Whishaw, I.Q. (2000). On the origin of skilled forelimb movements. Trends Neurosci. *23*, 372–376. https://doi.org/10.1016/S0166-2236(00)01618-0.
108. Katz, B. (1949). The efferent regulation of the muscle spindle in the frog. J. Exp. Biol. *26*, 201–217. https://doi.org/10.1242/jeb.26.2.201.
109. Gray, E.G. (1957). The spindle and extrafusal innervation of a frog muscle. Proc. R. Soc. Lond. B *146*, 416–430. https://doi.org/10.1098/rspb.1957.0021.
110. Jaeger, E.C.B., Vijatovic, D., Deryckere, A., Zorin, N., Nguyen, A.L., Ivanian, G., Woych, J., Arnold, R.C., Gurrola, A.O., Shvartsman, A., et al. (2025). Adeno-associated viral tools to trace neural development and connectivity across amphibians. Dev. Cell *60*, 794–812.e6. https://doi.org/10.1016/j.devcel.2024.10.025.
111. Lust, K., and Tanaka, E.M. (2025). Adeno-associated viruses for efficient gene expression in the axolotl nervous system. Proc. Natl. Acad. Sci. USA. *122*, e2421373122. https://doi.org/10.1073/pnas.2421373122.
112. Martin, P. (1990). Tissue patterning in the developing mouse limb. Int. J. Dev. Biol. *34*, 323–336.
113. DeLay, B.D., Corkins, M.E., Hanania, H.L., Salanga, M., Deng, J.M., Sudou, N., Taira, M., Horb, M.E., and Miller, R.K. (2018). Tissue-Specific Gene Inactivation in Xenopus laevis: Knockout of lhx1 in the Kidney with CRISPR/Cas9. Genetics *208*, 673–686. https://doi.org/10.1534/genetics.117.300468.
114. Schindelin, J., Arganda-Carreras, I., Frise, E., Kaynig, V., Longair, M., Pietzsch, T., Preibisch, S., Rueden, C., Saalfeld, S., Schmid, B., et al. (2012). Fiji: an open-source platform for biological-image analysis. Nat. Methods *9*, 676–682. https://doi.org/10.1038/nmeth.2019.
115. Letunic, I., Khedkar, S., and Bork, P. (2021). SMART: recent updates, new developments and status in 2020. Nucleic Acids Res. *49*, D458–D460. https://doi.org/10.1093/nar/gkaa937.
116. Letunic, I., and Bork, P. (2018). 20 years of the SMART protein domain annotation resource. Nucleic Acids Res. *46*, D493–D496. https://doi.org/10.1093/nar/gkx922.
117. Brinkman, E.K., Chen, T., Amendola, M., and van Steensel, B. (2014). Easy quantitative assessment of genome editing by sequence trace decomposition. Nucleic Acids Res. *42*, e168. https://doi.org/10.1093/nar/gku936.
118. Lin, T.-Y., Gerber, T., Taniguchi-Sugiura, Y., Murawala, P., Hermann, S., Grosser, L., Shibata, E., Treutlein, B., and Tanaka, E.M. (2021). Fibroblast dedifferentiation as a determinant of successful regeneration. Dev. Cell *56*, 1541–1551.e6. https://doi.org/10.1016/j.devcel.2021.04.016.
119. Fleming, S.J., Chaffin, M.D., Arduini, A., Akkad, A.-D., Banks, E., Marioni, J.C., Philippakis, A.A., Ellinor, P.T., and Babadi, M. (2023). Unsupervised removal of systematic background noise from droplet-based single-cell experiments using CellBender. Nat. Methods *20*, 1323–1335. https://doi.org/10.1038/s41592-023-01943-7.
120. Hao, Y., Stuart, T., Kowalski, M.H., Choudhary, S., Hoffman, P., Hartman, A., Srivastava, A., Molla, G., Madad, S., Fernandez-Granda, C., and Satija, R. (2024). Dictionary learning for integrative, multimodal and scalable single-cell analysis. Nat. Biotechnol. *42*, 293–304. https://doi.org/10.1038/s41587-023-01767-y.
121. Benaglia, T., Chauveau, D., Hunter, D.R., and Young, D. (2009). mixtools: An R Package for Analyzing Mixture Models. J. Stat. Softw. *32*, 1–29. https://doi.org/10.18637/jss.v032.i06.
122. Ignatyev, Y., Papadopoulos, S., Soretić, M., Yeung, J., Lin, T.-Y., Tanaka, E.M., Peshkin, L., Levine, A.J., Gabitto, M.I., and Sweeney, L.B. (2025).

Innovations in spinal cord cell type heterogeneity across vertebrate evolution. Preprint at bioRxiv. https://doi.org/10.1101/2025.10.09.680955.

123. Matsumoto, K., Mitani, T.T., Horiguchi, S.A., Kaneshiro, J., Murakami, T.C., Mano, T., Fujishima, H., Konno, A., Watanabe, T.M., Hirai, H., and Ueda, H.R. (2019). Advanced CUBIC tissue clearing for whole-organ cell profiling. Nat. Protoc. *14*, 3506–3537. https://doi.org/10.1038/s41596-019-0240-9.

124. Kroll, K.L., and Amaya, E. (1996). Transgenic Xenopus embryos from sperm nuclear transplantations reveal FGF signaling requirements during gastrulation. Development *122*, 3173–3183. https://doi.org/10.1242/dev.122.10.3173.

STAR★METHODS

KEY RESOURCES TABLE

REAGENT or RESOURCE	SOURCE	IDENTIFIER
Antibodies		
Acetylated Tubulin (Guinea Pig, polyclonal, 1:1k)	Sigma	Cat #: T6793; RRID:AB_609894
Islet1/2 (mouse, monoclonal, 1:25)	DSHB	Cat# 39.4D5; RRID:AB_2314683
Calbindin (mouse, monoclonal, 1:500)	Swant	Cat# CB300PUR; RRID: AB_3542811
Chx10/Vsx2 (guinea pig, polyclonal, 1:4k)	Sweeney Lab	Cat# CU2054; RRID: AB_3720853
Dmrt3 (rabbit, polyclonal, 1:4k)	Columbia University	Cat# CU1078; RRID: AB_3720849
MafB (rabbit, polyclonal, 1:4k)	Sigma	Cat# HPA005653; RRID:AB_1079293
GFP (chicken, polyclonal, 1:30k)	Aves	Cat#GFP-1020; RRID:AB_10000240
RFP (rabbit, polyclonal, 1:2k)	Rockland	Cat# 600-401-379; RRID:AB_2209751
En1 (guinea pig, polyclonal, 1:10k)	Columbia University	Cat# CU1714; RRID:AB_3313271
FoxP1 (rabbit, polyclonal, 1:16k)	Columbia University	Cat# CU1025; RRID:AB_2631297
FoxP2 (goat, polyclonal, 1:500)	Santa Cruz Biotechnology	Cat# sc-21069; RRID:AB_2107124
Hb9 (guinea pig, polyclonal, 1:5k)	Columbia University	Cat# CU1633; RRID: AB_3661722
Lhx3 (mouse, monoclonal, 1:5k)	DSHB	Cat# 67.4E12; RRID:AB_2135805
MafA (rabbit, polyclonal, 1:16k)	Columbia University	Cat# CU1755; RRID:AB_2941769
Pou3f1/cScip (Guinea pig, polyclonal, 1:16k)	Columbia University	Cat# CU687/688; RRID:AB_2631305
Pou6f2 (rat, polyclonal, 1:8k)	Columbia University	Cat# CU1796; RRID:AB_2665427
Raldh2 (guinea pig, polyclonal, 1:32k)	Columbia University	Cat# CU1022; RRID: AB_3661741
Sp8 (rat, polyclonal, 1:4k)	Columbia University	Cat# CU1944; RRID:AB_3644212
Sp8 (rabbit, polyclonal, 1:64k)	Columbia University	Cat# CU1943; RRID:AB_3644213
Sp8 (rabbit, polyclonal, 1:8k)	Millipore	Cat# AB-15260; RRID:AB_877304
Myosin heavy chain (mouse, monoclonal, 1:200)	DSHB	Cat# MF20;RRID:AB_2147781
Lhx3 (guinea pig, polyclonal, 1:4k)	Pfaff Lab	PMID: 9865699
Lhx3 (rabbit, polyclonal, 1:20k)	Pfaff Lab	PMID: 9865699
FoxP4 (rabbit, polyclonal, 1:32k)	Columbia University	Cat#: CU1797; RRID:AB_3644215

(*Continued on next page*)

Continued

REAGENT or RESOURCE	SOURCE	IDENTIFIER
FoxP4 (rat, polyclonal, 1:4k)	Columbia University	Cat#: CU1798; RRID:AB_3661716
Nr3b3/Errg (mouse, monoclonal, 1:2k)	R&D Systems	Cat #: PP-H6812-00; RRID:AB_2100280
Nr3b3 (rabbit, polyclonal, 1:4k)	Evans Lab, SALK	PMID: 19965931
Otp (rat, polyclonal, 1:16k)	Columbia University	Cat#: CU1941; RRID:AB_3644216
Otp (rabbit, polyclonal, 1:2k)	Abcam	Cat# ab50897; RRID: AB_881808
Nr4a2 (Rabbit, polyclonal, 1:500)	Santa Cruz Biotechnology	Cat#: SC5568; RRID:AB_2267355
Phospho-smad (Rabbit, polyclonal, 1:1k)	Columbia University	Cat# CU503; RRID:AB_2631311
Donkey Anti-Mouse IgG (H + L), AF405-conjugated (donkey, polyclonal)	Abcam	Cat# ab175658; RRID:AB_2687445
AffinitiPure Donkey Anti-Mouse IgG (H + L), AF488-conjugated (donkey, polyclonal)	Jackson ImmunoResearch	Cat# 715-545-151; RRID:AB_2341099
AffinitiPure Donkey Anti-Mouse IgG (H + L), Cy3-conjugated (donkey, polyclonal)	Jackson ImmunoResearch	Cat# 715-165-151; RRID:AB_2315777
AffinitiPure Donkey Anti-Mouse IgG (H + L), Cy5-conjugated (donkey, polyclonal)	Jackson ImmunoResearch	Cat# 715-175-151; RRID:AB_2340820
AffinitiPure Donkey Anti-Rat IgG (H + L), Cy3-conjugated (donkey, polyclonal)	Jackson ImmunoResearch	Cat# 712-165-153; RRID:AB_2340667
AffinitiPure Donkey Anti-Rat IgG (H + L), Cy5-conjugated (donkey, polyclonal)	Jackson ImmunoResearch	Cat# 712-175-153; RRID:AB_2340672
AffinitiPure Donkey Anti-Guinea Pig IgG (H + L), 488-conjugated (donkey, polyclonal)	Jackson ImmunoResearch	Cat# 706-545-148; RRID:AB_2340472
AffinitiPure Donkey Anti-Guinea Pig IgG (H + L), Cy3-conjugated (donkey, polyclonal)	Jackson ImmunoResearch	Cat#706-165-148; RRID:AB_2340460
AffinitiPure Donkey Anti-Rabbit IgG (H + L), 488-conjugated (donkey, polyclonal)	Jackson ImmunoResearch	Cat# 711-545-152; RRID:AB_2313584
AffinitiPure Donkey Anti-Rabbit IgG (H + L), Cy3-conjugated (donkey, polyclonal)	Jackson ImmunoResearch	Cat# 711-165-152; RRID:AB_2307443
AffinitiPure Donkey Anti-Rabbit IgG (H + L), Cy5-conjugated (donkey, polyclonal)	Jackson ImmunoResearch	Cat# 711-175-152; RRID:AB_2340607
Donkey Anti-Goat IgG (H + L), AF405-conjugated (donkey, polyclonal)	Abcam	Cat# ab175665; RRID:AB_2636888
AffinitiPure Donkey Anti-Goat IgG (H + L), AF488-conjugated (donkey, polyclonal)	Jackson ImmunoResearch	Cat# 705-545-147; RRID:AB_2336933
AffinitiPure Donkey Anti-Goat IgG (H + L), Cy3-conjugated (donkey, polyclonal)	Jackson ImmunoResearch	Cat# 705-165-147; RRID:AB_2307351
AffinitiPure Donkey Anti-Goat IgG (H + L), Cy5-conjugated (donkey, polyclonal)	Jackson ImmunoResearch	Cat# 705-175-147; RRID: AB_2340415
Bacterial and virus strains		
None	None	None
Biological samples		
None	None	None
Chemicals, peptides, and recombinant proteins		
O.C.T	Fisher Scientific	Cat# 23730571
Superfrost Plus slides	Fisher Scientific	Cat# 1367811E

(*Continued on next page*)

Continued

REAGENT or RESOURCE	SOURCE	IDENTIFIER
Normal donkey serum	The Jackson Laboratory	Cat# 017-000-121
Triton X-100	Sigma-Aldrich	Cat# T8787
L-Cysteine	Sigma-Aldrich	Cat# C7780-500G
ProLong Diamond	Invitrogen	Cat# P36970
ProLong Diamond with DAPI	Invitrogen	Cat# P36971
Cover glasses, 1.5 mm thickness	Fisher Scientific	Cat# 22266882
2-methylbutane	Sigma-Aldrich	Cat# M32631
DAPI	Sigma-Aldrich	Cat# D9542-1MG
PVA Mounting Medium with DABCO	Millipore Sigma	Cat# 10981
Paraformaldehyde (frog experiments)	Merck	Cat# 441344
Paraformaldehyde (mouse experiments)	Electron Microscopy Sciences	Cat# 15714
Triton X-100	Merck	Cat# 72593
TWEEN 20 (50% Solution)	Life Tech	Cat# 003005
Benzyl alcohol	Sigma-Aldrich	Cat# 402834-500ML
Benzyl benzoate	Sigma-Aldrich	Cat# B6630-250ML
Cas9 protein with NLS	PnasBio	Cat# CP01-200
Tissue freezing medium	Electron Microscopy Science	Cat# 72593
Gentamicin Sulfate	Sigma-Aldrich	Cat# G1914-5G
Dextran, Tetramethylrhodamine, 3000 MW, Anionic, Lysine Fixable	Sigma-Aldrich	Cat# D-3308
Cytiva Ficoll PM400	Fisher Scientific	Cat# 11590724
Gelatin from cold water fish skin	Sigma-Aldrich	Cat# G7041-500G
Pregnant Mare Serum Gonadotropin (PMSG)	Biozol	Cat# BVD-RP1782725000-5000
Chorionic Gonadotropin Human, Lyophilize (hCG)	Sigma-Aldrich	Cat# CG5-10VL
Cell membrane dye CellBrite® Blue	Biotium	Cat# 30024
Critical commercial assays		
Phire Tissue Direct PCR Master Mix	Thermo Fisher	Cat# F-170S
Deposited data		
Single-cell RNA sequencing data	This paper	GEO: GSE294631
Experimental models: Cell lines		
None	None	None
Experimental models: Organisms/strains		
Frog: wildtype pigmented *Xenopus laevis*	Institute of Science and Technology	N/A
Frog: *Xla.Tg(tubb2b:maptGFP)*^{Amaya}	EXRC	N/A
Frog: *Xla.Tg(218-2:GFP)*^{Swee}	This paper	218-2:GFP
Frog: *Xla.Tg(218-2:tdTomato; cry:tdTomato)*^{Swee}	This paper	218-2:tdT
Frog: *Xla.foxp1*^{tm1Swee}	This paper	N/A
Frog: *Xla.en1*^{tm1Swee}	This paper	N/A
Mouse: *En1::Cre*	The Jackson Laboratory	RRID:IMSR_JAX:007916
Mouse: *RC.lsl.Sun1-sfGFP*	The Jackson Laboratory	RRID:IMSR_JAX:021039
Oligonucleotides		
sgRNA sequences; See Table S2	This paper	N/A
Genotyping primers; See Table S1	This paper	N/A
HCR probes; See Table S5	This paper	N/A
Recombinant DNA		
N1_Slit3peGFP	This paper	SO04

(*Continued on next page*)

Continued

REAGENT or RESOURCE	SOURCE	IDENTIFIER
Slit:tdT_Cry tdT	This paper	SO57
Software and algorithms		
Xenbase illustrations	Xenbase	http://www.xenbase.org/; RRID:SCR_003280; https://scicrunch.org/resolver/SCR_003280/
Xenbase	Xenbase	http://www.xenbase.org/, RRID:SCR_003280; https://scicrunch.org/resolver/SCR_003280/
Adobe Illustrator	Adobe	https://www.adobe.com/at/products/illustrator.html
BIOP Cellpose QuPath Extension	–	https://zenodo.org/records/13752036
CellRanger v5.0.0	10x Genomics	https://github.com/10XGenomics/cellranger
CellBender v0.3.2	Broad Institute	https://github.com/broadinstitute/CellBender
CellPose (cyto2 model)	https://www.nature.com/articles/s41592-020-01018-x	N/A
R (v4.4.2)	The R Foundation	https://www.r-project.org/
Seurat v5 (R package)	Satija Lab	http://satijalab.org/seurat/
mixtools (R package)	Derek Young (via CRAN)	https://cran.r-project.org/web/packages/mixtools/index.html
Imaris 9.9.1	Oxford Instruments	https://imaris.oxinst.com/
MATLAB	Mathwords	https://www.mathworks.com/
Fiji 2.14.0	Schindelin et al.[114]	https://fiji.sc/
Prism 10-11	Graphpad Software, Inc.	https://www.graphpad.com/features
Python	https://www.python.org	v3.12.10
ZenBlue 3.7	Carl Zeiss Microscopy	N/A
Custom code for plotting neuron distribution	GitHub	https://github.com/tamachado/make_contours
SMART sequence analysis	Letunic et al.[115,116]	http://smart.embl-heidelberg.de/
SequenceBuilder Pro	DNASTAR	https://www.dnastar.com/software/lasergene/seqbuilder-pro/
TIDE 5.0.5	Brinkman et al.[117]	https://apps.datacurators.nl/tide/
BLAST	–	https://blast.ncbi.nlm.nih.gov/Blast.cgi
OBS (Open Broadcaster Software)	–	https://obsproject.com/
Marimo	https://marimo.io/	https://github.com/marimo-team/marimo
MATLAB	MathWorks	https://www.mathworks.com/products/matlab.html
QuPath	https://doi.org/10.1038/s41598-017-17204-5	N/A
Custom analysis pipeline for HCR signal quantification	This paper	https://git.ista.ac.at/iof-group/image-analysis/HCR-SpeckleQuantification (https://doi.org/10.5281/zenodo.18759665)
Code used for analysis of the single-cell data	This paper	https://github.com/yuriignatyev/V1sMNs_metamorphosis (https://doi.org/10.5281/zenodo.18683732)
Custom code for data analysis (including plotting neuron distribution, behavioral analysis, and Tadpose)	This paper	https://github.com/sweeneylab/MN_V1_analysis (https://doi.org/10.5281/zenodo.18755393)
Other		
Automatic capillary puller	Sutter Instrument	P-97

(*Continued on next page*)

Continued

REAGENT or RESOURCE	SOURCE	IDENTIFIER
Cryostat microtome	Bright	OTF 6000
Cryostat microtome	ThermoFisher	N/A
PicoSpritzer injection setup	World Precision Instruments	PV820
Standard Infusion Only Pump	Harvard Apparatus	70–4501
Glass capillaries	Drummond	3-000-203-G/X
Nikon CSU-W1	Nikon Instruments	CSU-W1
ZEISS LSM800	Carl Zeiss Microscopy	LSM800
ZEISS Lightsheet Z.1	Carl Zeiss Microscopy	Lightsheet Z.1
ZEISS Lightsheet 7	Carl Zeiss Microscopy	Lightsheet 7
ZEISS Apotome	Carl Zeiss Microscopy	N/A
Leica SP8 AOBS	Leica Microsystems	SP8 AOBS

EXPERIMENTAL MODEL AND STUDY PARTICIPANT DETAILS

Pigmented *Xenopus laevis* tadpoles were bred and raised at the Institute of Science and Technology Austria. Animals were maintained in specialized frog facilities, with the water temperature kept between 18°C and 22°C and a 12-h light:12-h dark cycle. All experimental procedures and animal husbandry followed protocols approved by the local authorities (permit number 2020–0.550.806, 2020–0.762.370, 2022–0.137.228, 2023–0.591.050 and 2024–0.019.606). Tadpoles were staged according to Nieuwkoop and Faber[26] and experiments were performed across developmental stages NF37 to juvenile frog stages. Sex cannot be reliably determined at the developmental stages used in this study; therefore, animals were used indiscriminately and sex was not considered as a biological variable. All mouse experiments were performed by the Jay Bikoff group in accordance with National Institutes of Health (NIH) guidelines and approved by the Institutional Animal Care and Use Committee (IACUC) of St. Jude Children's Research Hospital. Mouse tissues were collected from embryonic stage E13.5. Animals were housed on ventilated racks with controlled temperature and humidity, a 12-h light/dark cycle, and *ad libitum* food and water. Mice of both sexes were used for experiments; however, sex was not considered as a biological variable and no sex-specific analyses were performed.

METHOD DETAILS

Single cell RNA sequencing (scRNAseq)

Tissue collection, cells isolation and sequencing

X. laevis animals at swim stages (NF37-38 and NF47-48) and limb stages (NF54-55 and NF57-58) were used to generate single cell RNA-seq datasets. All animals, except for one replicate from NF57-58 batch, were transgenic *Xla.Tg(tubb2b:maptGFP)*^{Amaya} (EXRC), expressing GFP under neuron-specific *tubb2b* transcriptional control, enabling us to enrich neuronal cells. Spinal cord tissue was dissected from 295 NF47 to 48, 10 NF54-55, and 5–10 NF57-58 animals and pooled into 4 (NF47-48 and NF54-55) or 6 (NF57-58) technical replicates. At NF37-38, due to the small body size, the dorsal trunk was dissected from 230 animals, removing the belly and head at hindbrain boundary, and pooled into 4 total replicates. For all stages, acquired tissue was dissociated with liberase to obtain single-cell suspension according to previously published methods,[118] and FACS-sorted for the presence of GFP using a BD FACS Aria III Cell Sorter. Cells were then processed following the Chromium Single Cell 3′ v3.1 protocol and Chromium Reagent Kits were used to prepare single-cell libraries (10X Genomics). Sequencing was performed on a NovaSeq (Illumina).

Single cell data processing and quality control

10X CellRanger v5.0.0 was used for gene alignment to obtain gene-barcode matrices. The genome used for the reference was Xenla 9.2 (*X. laevis* v9). Ambient RNA was removed with CellBender v0.3.2 with 150 epochs and fpr of 0.01 from the raw features matrices produced by the cellranger function *count*.[119] Then, individual count matrices were imported into R (v4.4.2), converted into Seurat data object, and further analyzed with Seurat v5.[120]

To distinguish low-quality (dead) cells from viable cells, we modeled the distributions of UMIs/genes per cell on a log scale using a binomial mixture model (*mixtools*;[121]). This allowed us to distinguish viable cells from low-quality ones based on distribution overlap and guided us to assign thresholds for nFeature_RNA and nCount_RNA instead of choosing classical 'mammalian' thresholds for these values to make sure not to lose any good quality cells. These threshold choices were also confirmed with a high percentage of mitochondrial counts within 'low quality' cells. Low quality cells that did pass through chosen thresholds were further removed through clustering and differential expression analysis (see section below).

Cluster identification

For stage NF38, data was individually clustered and analyzed by marker gene expression to first identify neurons across all cells and then assign a cardinal class identity to neurons. A similar procedure was applied to stage NF54 (see also Ignatyev et al. for additional cross-species comparison of cardinal neuron identity).[122]

For each iteration (i.e., at all cells or neuronal level), the data was first normalized and scaled with *NormalizeData* and *ScaleData* functions. To perform the principal component analysis, we use *RunPCA* function on the basis of the most variable features in the data, which are defined with the function *FindVariableFeatures*. Then, we construct a k-nearest neighbor (KNN) graph with the function *FindNeighbors* based on the defined principal components and perform hierarchical clustering to group cells by their transcriptional proximity with the *FindClusters* function based on the KNN graph with different resolutions depending on whether neurons (coarse cell types) or cardinal neuronal classes within neuronal subset data (granular neural types) were being identified.

Clusters containing mixed identities in neuronal-level clustering (e.g., inhibitory V1 and dI6 neurons grouped together) were further refined by re-clustering and re-labeling to achieve a clearer and more accurate classification. Cluster and subcluster identities were validated by their expression of canonical cell- and neural-type markers, as well as differential expression analysis (*FindMarkers*, *min.pct = 0.25, logfc.threshold = 0.25*). Some re-clustered neuronal clusters were identified as contaminants and removed from downstream neuronal analyses. These included clusters that didn't express any cardinal class markers and either had high expression of oligodendrocyte markers (*plp1, mbp*) or noticeably low gene counts per cell and enrichment for mitochondrial and ribosomal genes. Final cell-type and neuronal subtype assignments were confirmed based on the expression of canonical markers of neurons and cardinal classes (Figures S5A, S5C, S5E, and S5G).

Label transfer

For stages NF47 and NF57, we used built-in Seurat's label transfer utilities to first identify neurons and then individual cardinal classes within the neuronal re-clustered data. Stage NF54 data was used as a reference to project its PCA embedding onto query datasets (NF47 and NF57). F*indTransferAnchors (LogNormalize)* and *TransferData* were used to map and assign cell types. The accuracy of these assignments was validated based on marker gene expression within the corresponding cell-type groups, both at the broad neuronal level and the finer cardinal class level (Figures S5B, S5D, S5F, and S5H).

Antibodies

The commercially available antibodies were obtained from the sources listed in the reagent table above. Additional antibodies against *Xenopus* proteins were generated in rat and rabbit at Covance using the following peptide sequences: *Xenopus laevis* OTP, CSSPDSSDVWRGSSIASLRRK (C-Term uniprot A0A1L8I213 (L) and A0A1L8HRF6 (S); Entrez gene 108717966 and 108707273); *Xenopus laevis* SP8 CHSPDLLHPPDRNGLE (C-Term uniprot Q5XGT8; Entrez Gene 495143); *Xenopus laevis* FoxP4 VGREGSGSGETNGELNPC (N-Term uniprot Q4VYR7; Entrez Gene 733240). *Xenopus laevis* Chx10/Vsx2 antibody was generated against GST fusion protein, comprising N-terminal BamHI and C-terminal XhoI sites cloned into pGex4T-2 (uniprot A0A8J0TBQ5; Entrez Gene 108698670).

Immunohistochemistry and microscopy of frog tissue

Spinal cord tissue was dissected and fixed in 4% paraformaldehyde (PFA) in phosphate buffer (w/v) for 90 min on ice, followed by cryoprotection overnight at 4°C in 15% sucrose-PBS solution containing 8% cold fish skin gelatin (w/v).

For antibody staining of sections, the tissue was embedded in tissue freezing medium, frozen on dry ice, and cryosectioned at 15 μm. Spinal cross sections were dried for 30 min at room temperature and then for another 4 h at 4°C. Once dry, sections were rehydrated with 1x PBS containing 0.2% Triton (PBST) for 2–5 min, washed another time with PBST, and left to incubate in primary antibody/PBST solution overnight at 4°C. Tissue was then washed three times with PBST. Secondary antibody incubation was performed in a dark chamber at room temperature for 30 min followed by three PBST washes. Sections were then mounted with 80–100 μL PVA/DABCO, coverslipped, and left to cure at room temperature for at least 2 h before imaging. Images of spinal sections were acquired at a confocal (ZEISS LSM800), spinning disk (Nikon CSU-W1) or widefield (ZEISS Apotome) microscope using a 20x objective.

For whole-mount immunohistochemistry, tadpoles were fixed in PFA, washed three times with PBS and once with PBS containing 0.1% Tween or 0.2% Triton (PBST). For BABB clearing, tissue was then incubated in the primary antibody mixture at 4°C for 4–6 days, washed three times in PBST, and incubated in the secondary antibody solution overnight. Tissue was washed in PBST three times and transferred into two parts benzyl benzoate and one part benzyl alcohol until clear. For CUBIC clearing, we adapted the protocol from Ueda Lab.[123] Briefly, directly after PFA fixation, tissue was washed three times in PBS and incubated in 50% CUBIC-L/R1a solution for three hours at room temperature, followed by incubation in 100% CUBIC-L/R1a for 2–4 days at 37°C. Tissue was washed 6 times with PBS, and immunostained as described above. Prior to imaging, tissue was transferred to CUBIC-R+(N) for refractive index matching. Cleared tadpoles were imaged using a lightsheet microscope (Figure 3I using ZEISS Lightsheet Z.1; Figures 4D and 4E using ZEISS Lightsheet 7).

Representative images of the spinal cord were obtained by creating maximum intensity projections from Z stacks using Zen (ZEISS) or Fiji softwares.

Immunohistochemistry and microscopy of mouse tissue

Adult pregnant female mice were deeply anesthetized via intraperitoneal injection of Avertin (Tribromoethanol, 240 mg/kg body weight) and then transcardially perfused sequentially with ice-cold PBS followed by 4% PFA (diluted in PBS). Individual embryos were not separately perfused. The spinal column was dissected and post-fixed overnight at 4°C, followed by cryoprotection in 30% sucrose (w/v) in 0.1M PB for at least 24 h at 4°C. Tissue was embedded in O.C.T., frozen, cryosectioned in the transverse plane at 10 μm, and mounted on Superfrost Plus slides. Immunohistochemistry was performed by blocking in 10% normal donkey serum and 0.3% Triton X-100, exposure to primary antibodies (guinea pig anti-En1 diluted at 1:16,000 in PBST, and chicken anti-GFP diluted at 1:30,000 in PBST) overnight at 4°C, and fluorophore-conjugated (Alexa Fluor Plus 488 or Alexa Fluor Plus 555) secondary antibodies for 1 h at room temperature. Sections were mounted using ProLong Diamond and coverslipped for imaging (Fisher Cover Glass, Cat# 22266882). Confocal images were acquired on a Leica SP8 AOBS (Leica Microsystems) confocal microscope using a 20x/0.8 NA objective. The positions of En1+ V1 neurons were identified using FIJI cell counter and plotted using custom MATLAB scripts (https://github.com/tamachado/make_contours). To account for variation in spinal cord size along the rostrocaudal axis, a representative spinal cord image was first reoriented in FIJI so that the dorsal edge of the spinal cord was parallel with the top of the image. All other spinal cord images were aligned and scaled to the reoriented image by using the FIJI registration plugin (Align Images Using Line ROI). First, a line was drawn between the dorsal and ventral edges of the spinal cord through the central canal. The plugin then uses the location, length, and angle of the obtained line to translate, scale, and rotate all other images.

Retrograde labeling

Prior to retrograde labeling, preoperative analgesia and anesthesia was administered to metamorphic tadpoles. Animals were placed onto a Tricaine-soaked gauze inside a sterile dish. Hindlimbs were severed at the limb base and crystals of Rhodamine Dextran were applied to the exposed area. After crystal application, tadpoles were placed into sterile 0.1x Marc's Modified Ringers (MMR) (recipe for 10x recipe: 1 M NaCl; 20 mM KCl; 10 mM $MgSO_4 \cdot 7H_2O$; 20 mM $CaCl_2 \cdot 2H_2O$; 1 mM EDTA; 50 mM HEPES, pH adjusted to 7.5) supplemented with 50 μg/mL gentamicin. Two days post-administration, tadpoles were fixed for further analysis.

Xenopus transgenesis

To induce ovulation, *Xenopus* females were pre-primed with 100 units of pregnant mare serum gonadotropin (PMSG; dorsal lymph sac injection) 3–12 days before egg laying, followed by priming with 1000 units of human chorionic gonadotropin (hCG; dorsal lymph sac injection) the day prior to egg collection. On the egg laying day, frogs were transferred into a tank filled with 1x egg laying solution diluted in MilliQ water (recipe for 10x stock: 1.2 M NaCl; 10 mM KCl; 24 mM $NaHCO_3$; 8 mM $MgSO_4 \cdot 7H_2O$; 300 mM Tris; 4 mM $CaCl_2 \cdot 2H_2O$; 3 mM $Ca(NO_3)_2 \cdot 4H_2O$, pH adjusted to 7.4–7.5 with concentrated HCl). Several hours after, eggs were collected, dejellied using 1x MMR solution containing 3% cysteine (pH 8.2), and subsequently washed twice in 1x MMR. Eggs were then transferred to agarose-coated dishes containing cold injection buffer (6% Ficoll, 0.5x MMR without Ca or EDTA). In parallel, sperm nuclei were prepared following the transplantation protocol outlined in Kroll et al.[124] Specifically, 4 μL of sperm nuclei preparation was incubated with 2.5 μL of linearized DNA plasmid (100 ng/μL) for 5 min at room temperature. This mixture was then combined with 16 μL of sperm dilution buffer and incubated for another 10 min at room temperature. The final mixture was diluted by resuspending 6 μL of the prepared sperm nuclei solution in 200 μL of sperm dilution buffer. For nuclear injections, we adapted the method from Kroll et al.[124] Briefly, glass capillaries were used to introduce the sperm nuclei mixture into unfertilized eggs. Following injection, the eggs were activated for 5 min in a calcium-ionophore-containing activation buffer (6% Ficoll, 0.5x MMR). Post-activation, embryos were thoroughly rinsed in post-injection buffer (1% Ficoll, 0.1x MMR). Cleaving embryos were subsequently transferred to 0.1x MMR supplemented with 50 μg/mL gentamicin and incubated at 15°C until the onset of gastrulation. Around NF40, GFP or tdTomato fluorescence was detectable in the hindbrain and spinal cord, enabling the selection of transgenic embryos. Genotype confirmation was performed via PCR genotyping (See Table S1 for primer sequences).

CRISPR-Cas9 knockout generation

Ovulation was induced as described above. Eggs were collected, rinsed with deionized water and *in vitro* fertilized using freshly dissected and smashed testis in 0.1x MMR. The embryos were then dejellied using 0.1x MMR solution containing 3% cysteine (pH 8.2), and subsequently washed twice in deionized water and twice in 0.1x MMR. Embryos were then transferred to petri dishes containing cold RNA injection buffer (1% Ficoll, 0.5x MMR) on a 16°C cold plate. Embryos were injected with either 3 or 16 ng of purified Cas9-NLS protein diluted in DNA-free water (Synthego), and 5 ng sgRNA (Synthego) either (i) twice into diagonally opposite points of the animal pole between 20 min and before cleavage to generate bilateral mutant animals, or (ii) once into only one cell at two-cell stage to generate unilateral mutant animals. Mutant and wild-type embryos were then moved to petri dishes containing 0.1x MMR supplemented with 50 μg/mL gentamicin and kept on a 16°C cold plate at least until the onset of gastrulation.

sgRNA design

To design sgRNAs, the mRNA and DNA sequences of both long and short isoforms of the gene of interest were taken from Xenbase. Single guide RNAs (sgRNAs) were designed using *Xenopus laevis* genome versions 9.2 or 10.1 with ChopChop (https://chopchop.cbu.uib.no/). sgRNAs were designed to target a 100% conserved region of the gene of interest in both short and long chromosomes. Additionally, sgRNAs were further selected such that the PAM site aligned with a highly conserved amino acid within this domain. sgRNA were synthesized *in vitro* at Synthego (https://www.synthego.com/). A full list of sgRNA sequences is presented in Table S2.

Xenopus laevis genotyping

To confirm the efficiency of the sgRNAs in generating bilateral and unilateral mutant animals, embryos were genotyped 2 days post fertilization. Each embryo was transferred in a separate Eppendorf tube with 100μL of 50 mM NaOH and boiled at 95°C–100°C for 15–30 min. After briefly vortexing the dissolved embryo, 15μL of Tris pH 8.8 was added and samples were centrifuged at 15,000 rpm at room temperature for 5 min and stored at −20°C. To obtain DNA material from mutant tadpoles and frogs, the animals were first anesthetized by transferring them to a 0.1x MMR with 0.01% tricaine solution and then the tail or the toe was clipped, and the tissue was processed in the same way as described above for the embryos. Mutant tadpoles and frogs were then moved to 0.1x MMR supplemented with 50 μg/mL gentamicin. The tail and hindlimbs of tadpoles and frogs were genotyped only after their final round of imaging.

The extracted DNA was then prepared for PCR, by adding 1x Phire Tissue Direct PCR master mix (Thermo Fisher), the forward and reverse primers necessary to amplify the gene of interest. The PCR primers and reaction conditions are as described in Tables S2 and S3, respectively. PCR products were Sanger sequenced using the reverse primer and mutation rate was estimated using TIDE analysis software.[117] For juvenile TIDE analysis estimation, the genomic DNA for left and right hindlimbs was processed separately and TIDE results were averaged.

Behavioral setup and video recording

The recording chamber measures 94 cm (length) by 73 cm (width) by 130 cm (height). For recordings, a 60 frames-per-second high-resolution IDS Imaging uEye+ UI-3180CP-*M*-GL camera, positioned 35.5 cm perpendicularly above a pull-out transparent acrylic sheet where glass dishes are put for imaging, was used to simultaneously allow for up to 6 dishes (14 cm in diameter) to be imaged in parallel. Infrared light was generated from below by six 850nm infrared LED light sources with two light diffusers (semi-transparent acrylic sheets). Before recording, the lens aperture was adjusted so that all dishes were in focus, all setup specifications and camera calibration files can be found on our github repository.

Before imaging, larvae, tadpoles and frogs were staged according to Nieuwkoop and Faber anatomical criteria.[26] Metamorphic stages were split into seven bins according to their anatomical features (NF37-37, NF44-48, NF52-55, NF57-58, NF59-62, NF63-64 and juvenile, which included animals from NF65 to less than 2.5 cm long froglets). For NF37-38, 5–10 animals were put per dish containing 100 mL of 0.1x MMR, whereas for all other stages only one animal per dish was put in 180 mL of 0.1x MMR. The animals were left for 15 min in the dishes to adapt to the behavioral setup conditions, and were then recorded using OBS Studio software while freely moving for two hours (2 times 1-h videos per animal). Raw videos containing multiple dishes were cut into videos containing only one dish using a custom-made MATLAB script to generate an undistorted image to correct for camera distortion and Fiji to draw a 800 × 800 pixel region of interest around individual dishes.

Videos were then subject to pose-estimation by the deep learning algorithm SLEAP.[24,25] For each stage bin, two SLEAP models were trained: a centroid model to quantify general features of tadpole-to-frog movement and a centered model to score kinematic features of the limbs and tail (Figures S1C and S1D). As larval tadpoles were small and largely stationary, multi-animal SLEAP detection and tracking was used at NF37-38 to capture a sufficient number of movement episodes[25]; single-animal SLEAP pose estimation was used for all other stages.[24] Centroid models for each stage tracked the center point of the body across frames, whereas centered models tracked a fixed number of points along the length of the tail and a single point for each limb joint. For the centered model, the following tail and/or limb points are tracked: eight tail points for NF44-48; 12 tail points for NF52-55; 12 tail, 10 hindlimb points for NF57-58; 12 tail, 10 hindlimb, 8 forelimb points for NF59-62 and NF63-64; 1 tail, 10 hindlimb, 8 forelimb points for juvenile stage.

Pose estimation by SLEAP

To predict the pose of tadpoles and frogs the SLEAP framework was used (ver. 1.2.9). For all stage bins, we applied a multi-animal top-down approach. In the centroid model we applied an input scaling of 0.5 on the gray-value movies. For training, an UNet backbone with max-stride of 16 and output-stride of 2 was selected. The Gaussian sigma for the central body-part was set to 3 (px). The number of filters was 16 with a filter-rate of 2. We used a middle block and up-interpolation. For training data augmentation random rotation, horizontal flips, scale and brightness with their corresponding default parameters were chosen. We trained for 400 epochs with a batch size of 8 and plateau patience of 40.

The centered-instance model was trained with no input scaling using an UNet backbone with max-stride of 32 and output-stride of 1 was selected. The number of filters was 32 with a filter-rate of 2. The Gaussian sigma for the body-parts was set to 5 (px). We used a middle block and up-interpolation. For training data augmentation rotation, random horizontal flips, scale and brightness with their corresponding default parameters were chosen. We trained for 800 epochs with a batch size of 8 and plateau patience of 60. In addition, online mining with a minimum of 2 hard key-points was selected. We used 10% of the training frames for validation and only the best model regarding the validation error was kept after training.

We manually annotated 448 frames for NF37-38, 607 frames for NF44-48, 451 frames for NF52-55, 405–499 frames for NF57-58, 405–457 frames for NF59-62, 250 frames for NF63-64, 405–410 frames for juvenile; the training was done on an AMD Ryzen 5950 × 16-Core workstation equipped with an Nvidia A4000 GPU having 16 GB of VRAM.

To track the detected poses of tadpoles and frogs, we used SLEAP's default centroid tracker using the Hungarian method for instance matching in a frame window of size 5.

The prediction and tracking of the recorded videos have been done with the SLEAP framework (ver. 1.2.9/1.3.3) on the institute SLURM HPC cluster using a custom submission script. The SLEAP output was converted to HDF5 for down-stream processing.

Our models achieved high levels of pose estimation accuracy as measured by quality control metrics such as average distance, visual recall, visual precision, object keypoint similarity (OKS) and mean precision per keypoint (mPCK) (Table S4). The average distance metric indicates the localization accuracy of predicted and manually annotated key points across the validation set. The overall keypoint detection accuracy is reflected by the Visual Recall and Visual Precision metrics. OKS metrics indicated the accuracy of the model overall, with higher numbers indicating better accuracy. Finally, mPCK metric provides information about the accuracy of the model to predict individual keypoints and is calculated as a percentage of predicted key points that are within 5 pixels from the manually annotated ones.

Quantification of behavior

Locomotion analysis

Locomotion features extract information about the basic movement of an SLEAP-tracked body-part. We partitioned the time-course of a tracked animal into *moving* and *non-moving episodes.* First, we extracted the xy-locations of the central body part from the SLEAP analysis HDF5 file. If the body-part was not detected in all frames, we linearly interpolated the missing frame locations using numpy.interp. Next, we applied a Gaussian smoothing to the x and y body-part locations using skimage.filters.Gaussian, with the sigma set to 1. The resulting smoothed locations are used to compute the instantaneous speed by central differences with numpy.-gradient. We then smoothed the resulting speed with a Gaussian with sigma = 30. Each frame is associated with a speed in pixels per frame, which we calibrated to cm per sec using the known diameter of the dish and the camera speed. Each dish was manually annotated with a circle ROI in ImageJ/Fiji. Finally, we thresholded the calibrated speed with a manually chosen threshold of 1.2 cm/s to obtain a binary partitioning into moving vs. non-moving animal episodes.

To compute the instantaneous speed and acceleration the central difference was used. For acceleration only the forward (positive) acceleration values were considered. In addition to the time spent moving per hour and the total distance, we computed various statistics of the instantaneous speed, acceleration and directional change.

To measure directional change, the angle between two succeeding time-points was computed. The angle at time t_i is defined by the locations P_i of the selected body-part. The angle was computed from two segments $\overline{P_{i-1}P_i}$ and $\overline{P_iP_{i+1}}$. The angle is 0 if the segments are parallel and ranges from -180 to 180°. To get a more robust signal to noise in the body part localizations, the raw xy-locations were smoothed with a Gaussian with sigma = 1. In addition, the time was sub-sampled using a factor of 8. All angles were given in degrees.

To calculate the area explored by each animal, we measured the ratio of dish area explored by the frog by selecting a central SLEAP-tracked body-part and building the 2D histogram of its trajectory. The square containing the circular dish ROI was discretized into 128 × 128 2D bins of size 1.09 × 1.09 mm. The 2D location histogram of the selected body-part is built over these bins. Each bin contains the number of times the location of the body-part was overlapping with this bin over its trajectory. Hence, a bin with value zero was never *visited*. The ratio of area explored is built by the number of bins visited divided by the total number of bins. To make movies of different length comparable, we further normalize this ratio to per hour.

Feature	Description
speed_moving_mean	mean of the instantaneous speed while moving (cm/s)
time_spend_moving_percentage	ratio of moving and the total number of frames (au)
directional_change_mean	mean of the directional change (degree)
directional_change_pos_mean	mean directional change regarding positive angles only
directional_change_neg_mean	mean directional change for regarding negative angles
acceleration_mean	mean positive acceleration
total_distance	total distance traveled while moving

Angle range and correlation analysis

Angle range features extract statistics of angle distributions at selected body-part segments. We defined several body-part segments where angles are computed in range (-180, 180) degrees, where an angle of 0° indicates parallel segments. Statistics of the angle ranges are partitioned from moving and non-moving episodes.

Angle Correlation features extract the correlation of angles measured at two pairs of body-part segments in a time resolved manner. The correlation was computed as windowed Pearson correlation. From the correlation coefficient distribution (during *active episodes*) several statistics were extracted.

First, angles at two pairs of body-part segments are computed. Both series of raw angles A and B were first smoothed with a Gaussian of sigma = 1 using scipy.ndimage.Gaussian_filter1d function. Then, the *Z* score of the smoothed angles values were computed. The *Z* score subtracts the mean and divides by the standard deviation to center the angle values around zero with unit variance.

To define *active episodes*, where the angle series have enough variance to compute meaningful correlations, we computed the gradient magnitude of the smoothed angle z-scores for A and B using central differences with numpy.gradient. The gradient magnitude involves a second Gaussian smoothing of sigma = 15.

The maximum over both gradient magnitudes were computed and thresholded with 5.73. Only correlations from time frames exceeding this threshold were used to compute the angle correlation distribution.

The correlation is computed by a centered, rolling Pearson cross-correlation using a pandas.rolling(win, center = True).corr() where inputs are the smoothed and z-scored input angle time series. From the resulting correlation distribution ranging $\in$ [-1,1] several statistics were extracted. We used a window size of win = 31 (frames) for the windowed cross-correlation.

Feature	Description
angle_moving_std	std of angles during moving episodes (degree)
angle_moving_mean	mean of angles during moving episodes
corr_median	median of the correlation distribution

Frequency analysis

Frequency features extract information about frequency of angle changes at specified body-part segments. The frequency is estimated using continuous Wavelet transform using the python module PyWavelets (ver. 1.4.1). Frequency bins (*n* = 24) were chosen in the range [0.937, 30] Hz with each bin being a factor of 1.16263 higher than the previous bin, and 30 Hz is the Nyquist limit for the recordings with a camera frame rate of 60 Hz.

We used the complex valued Morlet (Gabor) wavelet function for frequency estimation cmorl1.5–1.0, where cmorB-C with floating point values *B* = 1.5*, C* = 1.0 is given by:

$$\psi(t) = \frac{1}{\sqrt{\pi B}} e^{\frac{-t^2}{B}} e^{j2\pi Ct}$$

where *B* is the bandwidth and *C* is the center frequency.

We defined several body-part segments, from which angle frequencies are estimated and statistics of the power spectrum density (PSD) are extracted during *active episodes*.

As the tail mean power spectrum displayed a bimodal distribution, the frequency spectra were subdivided into low (0.9–4.5 Hz) and high (4.5–20 Hz) bins to estimate movement within each bin more accurately.

To define active episode, all angles are preprocessed by slightly smoothing with a Gaussian with sigma = 0.1, followed by computing the *Z* score. The preprocessed angle values are first smoothed with a Gaussian of sigma = 15 using scipy.ndimage.Gaussian_filter1d function. Then, the gradient magnitude is computed using central differences with numpy.gradient. The resulting magnitude is thresholded with 5.73. Only frequency estimates (mean power spectral density) from time frames exceeding this threshold are used to compute the mean PSD distribution.

To estimate angle change frequencies, we applied a continuous wavelet transform implemented in the PyWavelets function pywt.cwt. To obtain the power spectral density (PSD), we computed the magnitude by multiplying the wavelet coefficients with their complex conjugate. The time-resolved PSD is averaged in *active episodes* as described above.

Peak finding on the mean power spectral density is applied using the function scipy.signal.find_peaks to obtain the dominant frequency bin. The dominant frequency hence corresponds to a local maxima in the mean power spectral density (PSD). The prominence of a peak at the dominant frequency bin measures how much a peak *stands out* from the surrounding baseline of the signal and is defined as the vertical distance between the peak and its lowest contour line. The analysis is repeated for frequency ranges below and above a manual set frequency threshold of 4.5 Hz.

To remove spurious low frequency content, we optionally applied background subtraction to the smoothed angle z-scores. The background is estimated by smoothing the signal with a Gaussian of sigma = 15.

Feature	Description
dominant_freq	dominant frequency: local maximum frequency
dominant_freq_prominence	prominence of the dominant frequency peak
dominant_freq_power	mean PSD in active episodes at the dominant_freq
dominant_freq_X-	same as above, for frequencies <4.5 Hz
dominant_freq_prominence_X-	same as above, for frequencies <4.5 Hz

(*Continued on next page*)

Continued

Feature	Description
dominant_freq_power_X-	same as above, for frequencies <4.5 Hz
dominant_freq_X+	same as above, for frequencies >4.5 Hz
dominant_freq_prominence_X+	same as above, for frequencies >4.5 Hz
dominant_freq_power_X+	same as above, for frequencies >4.5 Hz
sum_psd_X-	sum of mean PSD for frequencies <4.5 Hz
sum_psd_X+	sum of mean PSD for frequencies >4.5 Hz

Animal pose visualization using PCA

To visualize typical configuration of frog body-part poses and their variance, we employed unsupervised dimensionality reduction using Principal Component Analysis (PCA). First, we aligned the animal pose into ego-centric coordinates. We centered the body-part *Tail_1 or Tail_Stem* as the origin and rotationally aligned body-part *Heart_Center* with the positive y axis using the Euclidean transformation implemented in the Python library scikit-image (ver. 0.22). Then, from the aligned coordinates a minimum 8000 skeletons body-parts of interest are sampled randomly and normalized to zero mean and unit variance for the PCA analysis. We used the first principal component to color-code the line segments of leg and tail poses for 256 randomly sampled frames.

Extraction of straight-line movement episodes

To identify episodes in which animals moved along a straight line from NF57-58 to juvenile stages, we aligned the body-axis with the movement direction. In every frame of each video, we calculated the body-axis unit vector by subtracting the Heart_Center from the Tail_1 (for stages from NF57-58 to NF63-64) or Tail_Stem (for juvenile stage) and normalizing it to unit length. The movement displacement vector was determined using central differences with the numpy.gradient function on the Tail_Stem body part at each frame, followed by normalization.

Subsequently, we calculated the dot products of all body-axis and displacement vectors using the numpy.vecdot function. The resulting vector correlations, which ranged from −1 to 1, were interpreted as follows: values near −1 indicates backward movement, values near 1 suggests forward movement, and values close to zero denotes sideways movement. To reduce noise, the vector correlations were processed with a temporal median filter spanning 3 frames (0.05 s) using the one-dimensional scipy.ndimage.median_filter function.

Candidate straight-line movement episodes were then identified by applying a correlation threshold of at least 0.8, corresponding to an angular deviation between 0° and 36.9°. We employed the skimage.measure.label function to identify temporally contiguous episodes post-thresholding. For subsequent analyses, only episodes with a minimum duration of 90 frames (1.5 s) were retained.

Finally, for each candidate episode, we computed the average speed and trajectory confinement ratio. The confinement ratio is defined as the net Euclidean distance between the start and end positions divided by the total trajectory length. Episodes selected for further analysis had to exhibit a minimum speed of 1.2 cm/s for all stages and a confinement ratio greater than 0.95. Implementation was done in a custom Python 3 Jupyter notebook using the numpy (ver. 2.2.6), scikit-image (ver. 0.25.2) and scipy (ver. 1.15.3) libraries. Example montage videos of straight-line moving episodes were generated using moviepy (ver. 2.2.1).

QUANTIFICATION AND STATISTICAL ANALYSIS

Behavioral tracking statistics

Statistical quantification of the behavioral data obtained from our Tadpose analysis was done only on videos with a minimum of 90% tracked frames and considering only moving episodes for overall animal movement and active episodes for tail and limb kinematics quantification. ROUT outlier test was first applied to each dataset and outlier values removed. Then, each dataset was checked for normal distribution using D'Agostino & Pearson test, Anderson-Darling test, Shapiro-Wilk test, Kolmogorov-Smirnov test as appropriate. Data is assumed to not have the same variance. For comparison between two datasets, if the data was normally distributed, an unpaired *t* test with Welch's correction was applied, otherwise a Mann-Whitney test was used. For comparison between three or more datasets, if the data was normally distributed, a Brown-Forsythe and Welch ANOVA test was applied, otherwise a Kruskal-Wallis test was used. The *p*-values were defined as follows: <0.05 (*), <0.01 (**), <0.001(***), <0.0001 (****).

All plots for percentage of time moving, distance traveled, speed, acceleration and turning, as well as mean and std angle, dominant frequency and sum power are shown as median with min and max values as dots, and first quartile and third quartile as box limits. Dots represent a bout of animal movement for NF37-38, as every time the animal touches the border of the dish it is considered as a different animal. For NF44 to juvenile stage animals, as each animal is recorded for two one-hour windows, two dots represent the same animal. For the limb kinematics analysis of wildtype and En1 ½ CRISPR movement, each animal during one-hour recording was sampled twice with left and right fore and/or hindlimb movement recorded separately and used as an independent data point. For FoxP1 ½ CRISPR analysis, left and right limbs were sampled separately. Mean power spectrum curves are plotted as the median between all data points for frequency bins sampled.

Cell-type quantification

Motor neurons and V1, V2a and dI6 interneuron (sub)populations were quantified in *Xenopus* using the spot detection function on full z-stacks within Imaris software. For marker co-expression analysis, a custom MATLAB script (https://github.com/sweeneylab/MN_V1_analysis) was used to identify colocalized nuclei within a 4.5 μm radius. These detection counts were then used to calculate the percentage of a given cell subset within the population. As a comparative reference, motor neuron counts for E13.5 mice[51] and V1 interneurons counts from P0 mice[11] were used.

Spatial plotting

During Imaris-based cell detection, three anatomical reference points were annotated in the spinal cord: the center (central canal), the bottom (most ventral point of the white matter), and the side (most lateral point of the white matter). These reference points enabled normalization of the detected cell positions, which were then plotted using a MATLAB script (https://github.com/sweeneylab/MN_V1_analysis) onto a spatially normalized P0 mouse spinal cord at either thoracic or lumbar levels.

Entropy analysis

To define and estimate the diversity and specialization of transcriptomes and gene specificity across developmental stages, we define transcriptome diversity using concepts of Shannon entropy of a gene frequency distribution at each developmental stage, based on the work of Martinez and Reyes-Valdez.[79] Gene specificity is defined as the mutual information between the tissues and the corresponding transcript. More specifically, we quantify transcriptome diversity using 9 TFs: FoxP1, FoxP2, FoxP4, MafB, Nr3b3, Nr4a2, Otp, Pou6f2, and Sp8. We created a measure Dj, of diversity in tissue j, which measures how much a given stage j departs from the transcriptomic distribution of all the stages under comparison. Dj = Hrj - Hj, where Hrj is the average log2 of the global transcript frequencies in a given tissue, and Hj represents an adapted entropy. They are calculated from the relative frequency of cells expressing each i TFs at stage j, pij, and the average frequency across stages pi, by the following expression: Hj = - \sum_i = 1 ˆG pij log(pij) and Hrj = - \sum_i = 1 ˆG pij log(pi).

Cell-type statistics

Cell-type data are presented as mean ± SEM in all graphs unless otherwise specified in Figure Legends. The normality of data distribution was assessed using the Shapiro-Wilk test.

For comparisons between two groups, Welch's *t* test was used for normally distributed data, and Mann–Whitney test for non-parametric comparisons. For comparisons across multiple groups, Brown-Forsythe and Welch ANOVA or ordinary one-way ANOVA were used for normally distributed data, followed by Šídák multiple comparisons tests where appropriate. For non-normally distributed data, the Kruskal–Wallis test was used, followed by Dunn's multiple comparisons test when required. For analyses involving two independent variables, two-way ANOVA followed by Šídák multiple comparisons tests or uncorrected Fisher's Least Significant Difference tests was used. The *p*-values were defined as follows: <0.05 (*), <0.01 (**), <0.001(***), <0.0001 (****).

In Figure 3, cell counts were log-transformed using base 10 ($\log_{10}$) prior to statistical analysis. This transformation was applied to account for a wide range of cell numbers observed across developmental stages and spinal cord levels, ensuring the data conformed more closely to assumptions of normality and homoscedasticity. All statistical analyses were performed using GraphPad Prism software.

HCR quantification

Fluorescent multiplex *in situ* hybridization using Hybridization Chain Reaction (HCR v3.0, Molecular Instruments, Inc.) was performed on spinal cord tissue from NF54 wild-type (WT) and unilateral En1 CRISPR mutant animals. For En1 mutant analysis, animals were first processed for immunohistochemistry (IHC) against En1 to confirm mutant status via loss of En1 protein expression. Only IHC-confirmed mutants were included in subsequent HCR experiments. HCR labeling was performed using five probe combinations: each included *en1* (V1 marker), *foxd3* (a proxy marker for a broader V1/dI2 population), and one of five V1 clade or subset markers (*nr5a2, pou6f2, foxp2, sp8, or mafa).* Oligo pool sequences for each mRNA (Integrated DNA Technologies) are provided in Table S5. Probes targeting each mRNA were hybridized overnight at 37°C, followed by amplification according to the manufacturer's protocol. Following HCR labeling, a subset of samples was incubated with a cell membrane dye (CellBrite Blue; Biotium, #30024) for 15 min according to the manufacturer's instructions to visualize cell boundaries. All sections were subsequently covered mounted in 80–100 μL PVA/DABCO, coverslipped, and allowed to cure for several hours prior to imaging.

Images were acquired using spinning disk confocal microscopy (Nikon CSU-W1) with a 40× water immersion objective (1.15 NA), with optical sections acquired every 0.4 μm through the entire thickness of each section. Entire Z-stacks were used for quantification.

Quantification was performed using a custom analysis pipeline combining QuPath, CellPose, and Python. All sections were subjected to quality control. Sections with poor segmentation (<1600 detected cells) or low HCR signal for the control gene foxd3 (<10% positive cells per hemisection) were excluded from downstream analyses. For retained sections, positive cell counts were divided by total number of detected cells (% positive cells per hemisection) to compare across sections of varying size and cell number.

In detail, raw images were exported and processed with a custom Fiji macro to include manual annotation of regions of interest (ROIs) and channel sorting. Exported images were imported into QuPath where cellular boundaries were segmented using the CellPose cyto3 model using the BIOP Cellpose QuPath extension on the autofluorescence background channel imaged with the 405 nm excitation. Fluorescent RNA puncta corresponding to HCR signal speckles were detected using QuPath (v0.5.1) via userdefined thresholding pixel classifiers (https://qupath.readthedocs.io/en/stable/docs/tutorials/thresholding.html#thresholders-in-qupath). In Python (v3.12.10), the number of cells co-expressing each RNA probe combination was calculated per region of interest (ROI) as defined by the *en1*/*foxd3* expression. Final co-expression values were calculated based on the cell area coverage thresholds determined for individual channels (*en1* > 10%; *foxd3* > 10%; *foxp2* > 10%; *mafa* > 5%; *nr5a2* >25%; *pou6f2 > 10%*; and *sp8 > 10%*). A custom interface was built using Marimo to run the QuPath analysis and subsequent Python steps in a routine manner.

HCR quantification statistics

For comparisons between two genotypes, unpaired t-tests were used for normally distributed data, and Mann–Whitney tests when data did not meet assumptions of normality. All statistical analyses were performed using GraphPad Prism software. The *p*-values were defined as follows: <0.05 (*), <0.01 (**).